Resonant MEMS Deformable Mirror

by

Samed Kocer

A thesis
presented to the University of Waterloo
in fulfillment of the
thesis requirement for the degree of
Master of Applied Science
in
Systems Design Engineering

Waterloo, Ontario, Canada, 2021

© Samed Kocer 2021

Author's Declaration

I hereby declare that I am the sole author of this thesis. This is a true copy of the thesis, including any required final revisions, as accepted by my examiners.

I understand that my thesis may be made electronically available to the public.

Abstract

The performance of optical systems is often affected by aberrations that degrade the image resolution and contrast. These aberrations may be induced from atmospheric turbulence, imperfection in the optical alignment, or inhomogeneous refractive index distribution. Adaptive optics (AO) technology has been incorporated into different types of imaging instrument to correct optical aberrations. Deformable mirrors (DMs) are commonly used correction elements in AO due to their high optical performance, low cost, and reflective characteristics which enable to operate at different wavelengths. A DM can correct the aberrations by introducing a counter deformation to its reflective surface with respect to aberrated wavefront. Various DM designs have been developed over the last several decades to improve the state-of-the-art.

Conventional DMs were invented to be used in astronomical observations. They are bulky, expensive, and required high voltages to operate. The development of micromachining introduced MEMS based DMs as an alternative to conventional ones and extended the utilization of AO in many areas including microscopy, laser machining, ophthalmoscopy, and optical coherence tomography (OCT). The design of DMs can be classified in two categories based on their reflective surface topology either segmented or continuous. Segmented DMs impose piston-tip-tilt motion to deform surface. They prevent cross coupling between actuators and provide high strokes, but the gaps between each segment scatter the light, and cause diffraction. Continuous DMs accomplish almost zero diffraction operation, however inter-actuator coupling occurs.

MEMS DMs are preferred due to their compact size, low power consumption, and relatively fast response time. Piezoelectric, electrostatic, electrothermal, and electromagnetic actuation mechanisms are applied via a distributed actuator array underneath a mirror surface to deform its profile. Majority of the MEMS DM designs have mainly built on direct current (DC) electrostatic or piezoelectric actuation mechanisms. The former are encumbered with high electrode counts, special control algorithms and associated hardware. The latter are encumbered with hysteresis and complex structure which reduces their compatibility to micromachining. Besides, piezoelectric MEMS DMs might not be able to correct high and low order aberrations in a single actuator array design. Therefore, different electrode schemes might be necessary to replicate higher order aberrations, and each scheme requires different fabrication.

Recent developments in AO have emphasized the demand for large stroke, low cost, easy-driven wavefront correction elements which built-in a simple miniaturized architecture to compensate optical aberrations rapidly in real-time. Thus, there is a need to develop such a system to advance the current state-of-the-art. In this thesis, we present a novel MEMS DM that can be used for AO to correct wavefront aberrations during real-time scanning. The DM employs resonant electrostatic actuation (REA) via 49 electrodes to deform a 1.6 mm circular plate dynamically. The DM surface was designed to be continuous to eliminate light diffraction across

the facesheet. Unlike bias actuated and piezoelectric DMs, it can correct both low and high order aberrations within a simple device structure using a single actuator array by applying a single voltage waveform, thereby eliminating the need for individually addressable electrodes and the use of complex influence functions. REA drives the mirror at resonance and exploits dynamic amplification to increase the stroke with a minimal number of electrodes. The mirror depicts a low cost and high-performance alternative to previous MEMS DMs.

The DM was designed and fabricated using a silicon-on-insulator (SOI) MEMS fabrication process. Finite element (FEM) simulations were conducted to determine natural frequencies and mode shapes of the DM geometry. Experimental characterization was carried out using laser Doppler vibrometer (LDV). To demonstrate mirror capability the DM was integrated into an optical system as a varifocal mirror to shift the focal point of a 532 nm incident pulsed laser beam. It is shown that an 8 cm focal shift was realized between the focal lengths of 11 cm and 19 cm. The DM surface was controlled easily by changing the phase angle ϕ between the pulse signal of the incident laser beam and the drive signal of the DM. The mirror promises to advance the current state-of-the-art aberration correction techniques and can be used as an adaptive element in AO systems for axial scanning and 3D multiwavelength imaging.

Acknowledgements

I would like to express my sincere gratitude and deepest appreciation to my supervisors Prof. Eihab Abdel-Rahman and Prof. Mustafa Yavuz for all their help, insightful guidance and immense knowledge. This work cannot be completed without their continuous support and encouragement. My sincere thanks to Prof. Parsin Hajireza for his help, contribution, and valuable feedback on my experimental results.

I would like to thank my thesis committee members, Prof. Bo Cui and Prof. Nasser Lashgarian Azad for their valuable feedback.

I am very grateful to my fellow researchers Lyazzat Mukhangaliyeva and Dr. Amr Kamel for their hard work, effort, and insightful contribution throughout this work.

I would like to thank my colleagues and lab mates Dr. Resul Saritas, Dr. Alaaeldin Elhady Ahmed, Dr. Mohamed Arabi, Ahmet Gulsaran, Dr. Kevan Bell, Muhammed Kayaharman, and Bersu Bastug Azer for all their help, contribution and collaborative works throughout my academic career. I am very appreciated for the stimulating conservations, for training me all the equipment that I use, and for creating a productive research environment at the University of Waterloo.

I would like to thank my roommates, Abdullah Ince, Yusuf Eryilmaz and Muhammed Kayaharman for their endless support, invaluable friendship and tolerance over the years.

I would like to express my special thanks and sincere gratitude to my mother, my father and my sister for their continuous support, and encouragement throughout my life.

Dedication

To my innocent brothers in arms who are sentenced to life imprisonment

and

our families

Table of Contents

List of Figures ix

List of Tables xii

1 Introduction 1

1.1 Background 1

1.1.1 Aberrations in Optical Systems 1

1.1.2 Adaptive Optics 6

1.1.3 Deformable Mirrors 9

1.2 Motivation and Objectives 17

1.3 The Outline of the Thesis 19

2 Design and Fabrication 20

2.1 Design Criteria 20

2.2 Mirror Design 22

2.3 FEM Analysis 24

2.3.1 Eigenfrequency Analysis 24

2.3.2 Static Analysis 24

2.3.3 Dynamic Analysis 25

2.4 Fabrication 26

2.5 Packaging 29

3 Experimental Characterization **31**
3.1 Experimental Setup 31
3.2 Modal Analysis 31
3.3 Curvature of the DM at Defocus Mode 35

4 Integration into Adaptive Optics **41**
4.1 Endurance of the DM 41
4.2 Optical Characteristics 43
4.3 Varifocal Mirror 45

5 Conclusions and Future Work **48**
5.1 Conclusions 48
5.2 Future Work 49

References **50**

List of Figures

1.1 a) A wavefront with no aberration, and b) with spherical aberration. 2

1.2 1) Ideal image, 2) Axial chromatic aberration, 3) Lateral chromatic aberration. . . 3

1.3 Ideal wavefront, aberrated wavefront, and light rays coming from infinity. 3

1.4 The first six order Zernike modes 4

1.5 The first five order Zernike modes and corresponding visual aberrations 6

1.6 Optical phase conjugation principle, a) A wavefront passed through disturbed medium, and it is aberrated. b) The conventional mirror reflected the aberrated wavefront, and it is aberrated once more when passing through disturbed medium. c) An aberrated wavefront is moving towards the DM. d) The reflected aberrated wavefront keeps its shape due to the DM, and when it passes through disturbed medium again, it has become corrected. 7

1.7 a) Open loop AO. b) Closed loop AO. 8

1.8 AO in a) astronomy, images of the double star 53 Bootes using Large Binocular Telescope without AO and with AO, b) microscopy, dentritic spines in mouse brains along the lateral and axial directions imaged without AO and with AO. . . 8

1.9 AO in a) ophthalmoscopy, images of the human photorecetotors of the left eye, and d) laser machining, images of graphitic wires beneath the surface of diamond using an ultrafast laser without AO and with AO. 9

1.10 Historical developments of the DM technology 10

1.11 Stacked array DM. 11

1.12 a) Segmented DM, b) Continuous DM. 12

1.13 a) Schematic of the DM, b) Actual device. 13

1.14 a) Schematic of the one segment, b) Actual device. 13

1.15 a) Schematic cross section of the continuous MEMS DM, b)The surface of the DM, and the 12×12 square electrode grids (w/o corners) 15
1.16 a) A schematic of the piezoelectric mirror membrane, and PZT actuators, b) Cross sectional schematic of the piezoelectric DM, c) SEM picture of the DM, and electrode arrays. Copyrights© 2006. IEEE. 16
1.17 a) A schematic of the varifocal piezoelectric MEMS DM, b) Cross sectional schematic of the varifocal piezoelectric MEMS DM. 17

2.1 a) Dimensions of the mirror plate and surrounding beams, b) Electrodes configuration, c) A schematic of the DM, d) Dimensions of the DM. 22
2.2 a) Dimensions of the mirror plate and surrounding beams, b) Electrodes configuration, c) A schematic of the DM, d) Dimensions of the DM. 23
2.3 Eight mirror plate mode shapes obtained from eigenfrequency analysis in COMSOL: a) Defocus at $f_1 = 23.95$ kHz, b) Primary coma at $f_2 = 57.07$ kHz, c) Astigmatism at $f_3 = 85.98$ kHz, d) Primary spherical at $f_4 = 105.6$ kHz, e) Trefoil at $f_5 = 111.9$ kHz, f) Secondary coma at $f_6 = 155.8$ kHz, g) Tetrafoil at $f_7 = 208.1$ kHz, and h) Secondary spherical at $f_8 = 242.0$ kHz. 24
2.4 Static deflection, w_s of center point of the mirror bottom surface as a function of voltage obtained from the FEM simulation. 25
2.5 Displacement time-history of center point of the mirror bottom surface under a sinusoidal actuation signal obtained from FEM simulation. 26
2.6 a) Substrate, b) Trench 1 and Trench 2, c) Y Mask, d) Metal deposition, e) Z Mask, f) Final layout 28
2.7 a) Patterning electrodes with DRIE etching (Trench 1, 51 µm, and Trench 2, 35 µm, b) Patterning mirror, support beams, and posts wit DRIE etching (Y Mask), c) Anodic bonding, d) Removing handle layer and buried oxide by wet etching on top wafer, e) Gold deposition 29
2.8 a) Chip carrier, b) Backside of the chip carrier, c) Wirebonded chip 30
2.9 a) The PCB used to reach each actuation electrodes individually, b) A microscopic picture of the DM 30

3.1 a) Schematic of the experimental setup, b) A picture of the experimental setup . 32

3.2 Measured responses to the applied impulses, a) Axisymmetric impulse, b) Circumferential impulse. Subsets of the each figure show the actuation scheme, and measurement locations on the mirror plate. 33

3.3 a) The frequency-response curve of the DM to a) an axisymmetric impulse, and b) a circumferential impulse 34

3.4 Experimental mode shapes obtained by using LDV, a) Defocus mode at $f_1 =$ 16 kHz, b) Primary coma at $f_2 = 43$ kHz, c) Astigmatism at $f_3 = 68$ kHz, d) Primary spherical at $f_4 = 81$ kHz, e) Trefoil at $f_5 = 87$ kHz, f) Tetrafoil at $f_6 =$ 105 kHz, g) Secondary coma at $f_7 = 122$ kHz, h) Secondary spherical at $f_8 =$ 187 kHz. 35

3.5 a) The point-grid used to measure the DM surface deformation., b) Numbering the grid points 36

3.6 a) Static response: The displacement time-history at 15 evenly spaced points under a 70.71 V step voltage, b) Dynamic response: The measured oscillations of the point-grid under a sinusoidal waveform with 100 V amplitude and 8 kHz frequency. 37

3.7 The DM surface along the point-grid diameter at 19 oscillation phase angles $\phi_{\text{oscillation}}$. 38

3.8 A comparison between the measured defocus and Zernike defocus using normalized values 39

3.9 RMS error between the theoretical Zernike defocus and the measured defocus. . . 40

4.1 The measurements of the power of the laser beam a) before, and b) after the DM. 42

4.2 Results of the endurance test of the DM, the black dot shows the place where the DM is burnt. 43

4.3 The measured value of the gold reflectivity. 44

4.4 a) Horizontal and b) vertical profiles of the laser beam reflected from the DM (red dots) compared to a Gaussian fit (blue line). Insets shows the 2D and 3D profiles of the reflected beam. 44

4.5 a) A schematic and b) a picture of the adaptive optics experimental setup. 45

4.6 Drive signal of the DM (red line), pulse signal of the laser beam (blue line), and DM displacement (black line) for a) $\phi_{\text{drive}} = 45°$ and b) $\phi_{\text{drive}} = 135°$. c) The measured beam waist of the reflected beam at 14 equally spaced points measured from the DM. 46

List of Tables

1.1 Optical Aberrations 2

2.1 Material properties of the crystalline silicon layers 27

2.2 Characteristics of the fabrication masks 27

3.1 The radius of curvature at the plate centre for a set of seven selected phase angles $\phi_{\text{oscillation}}$. 39

Chapter 1

Introduction

This chapter consists of four sections. The first section reviews the background information that establish the underlying logic behind the research. The motivation and research objectives are stated in the second and third sections. In the last section, the outline of the thesis is given.

1.1 Background

This section provides a review of optical aberrations which are the main source of performance degradations in imaging instruments. Then, AO is examined as a promising technology to correct the aberrations, and restore the performance of optical systems. Finally, DMs are introduced as the most common used adaptive correction elements in AO. In general, this section explains the motivation behind the proposed research.

1.1.1 Aberrations in Optical Systems

Aberrations are optical factors that reduce the image resolution and contrast by causing an optical system to react abnormally than the ideal behaviour. In an ideal case, the image should be similar to the object by focusing every object points to one image point [1], as shown in the Figure 1.1(a). However, aberrations cause diffraction which prevent the reflected light to focus in a single point1.1(b). Due to intrinsic nature of the optical systems, aberrations always exist and degrade their performance [2]. Optical aberrations can be categorized into two groups: chromatic aberrations and monochromatic aberrations [3]. Table 1.1 shows classification of the aberrations.

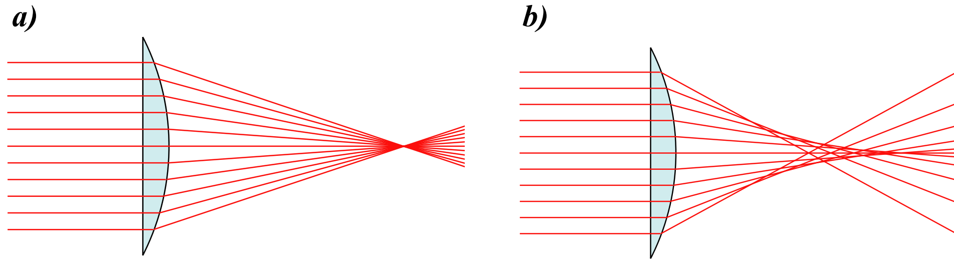

Figure 1.1: a) A wavefront with no aberration, and b) with spherical aberration [4]

Chromatic aberrations occur when different wavelengths or colours are not focused to the same point. If the focal points vary along the longitudinal distance, it is called axial chromatic aberration. If they vary along the vertical distance, it is called lateral chromatic aberrations [3, 5, 6]. Figure 1.2 illustrates the chromatic aberrations .

Chromatic Aberrations	Monochromatic Aberrations
Axial chromatic aberration	Defocus
Lateral chromatic aberration	Spherical aberration
	Astigmatism
	Coma
	Field curvature
	Image distortion

Table 1.1: Optical Aberrations

On the other hand, monochromatic aberrations originated from the geometry of the wavefront, and it can be occurred either when the light is reflected or when it is refracted. Monochromatic aberrations can manifest as defocus, spherical aberration, astigmatism, coma, field curvature, and image distortion [3, 5, 6, 7]. An ideal wavefront is a surface that is normal to the incident light rays coming from infinity with a constant phase [2]. As the light rays pass through the perfect refractive surface, they come together at the focal point. However, there is no such a case in the real world, and there is always distortions (phase change) along the surface which leads aberrations. Figure 1.3 shows the ideal and aberrated wavefronts for a plane and spherical surface.

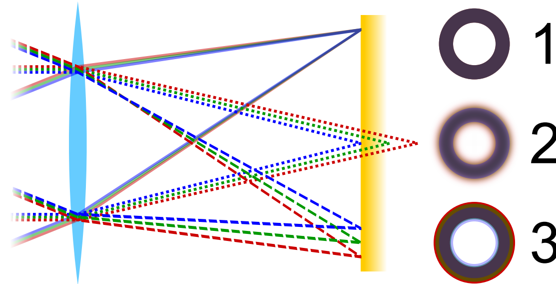

Figure 1.2: 1) Ideal image, 2) Axial chromatic aberration, 3) Lateral chromatic aberration [8].

Wavefront aberrations may arise from atmospheric turbulence, temperature variations, optical misalignments , and inhomogeneous refractive index distribution [9, 10, 11]. In astronomical applications, atmospheric turbulence creates inhomogeneities in the atmosphere by mixing the air layers that have different temperatures and density. Such a randomized mixing causes fluctuation in the refractive index of the atmosphere, and induces aberrations [12]. In microscopy, the resolution of the image is affected by the optical properties of the sample. Spatial variations across the refractive index of the specimen create diffraction, and limit the performance of the microscope [13]. The human eye also has wavefront aberrations due to the refractive index mismatch along the different layers of the cornea [14].

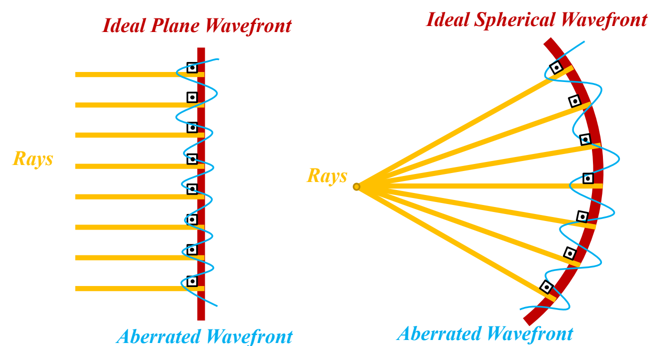

Figure 1.3: Ideal wavefront, aberrated wavefront, and light rays coming from infinity.

In ophthalmology, the distorted wavefront or aberration is often represented by Zernike polynomials that are a sequence of continuous and orthogonal polynomials over a unit circle. Most of the optical systems are using circular optical components which makes Zernike polynomials preference to model optical wavefront propagations in those systems. Fritz Zernike employed

them for the first time to develop phase-contrast microscopy in 1950s. In this mathematical representation, an arbitrary wavefront was modelled in terms of orthogonal Zernike polynomials, $Z_n^m(\rho, \phi)$, in the radial (n) and angular (m) directions. The values of n and m gives the required function to model that wavefront. Aberrations are ranked based on their radial order. If the radial order less than 3 ($n = 0, 1, 2$), it is called lower order aberrations. If the radial order equal or higher than 3 ($n \geq 3$), it is called higher order aberrations [15, 16, 17, 18]. The first six order of Zernike modes are shown in the Figure 1.4.

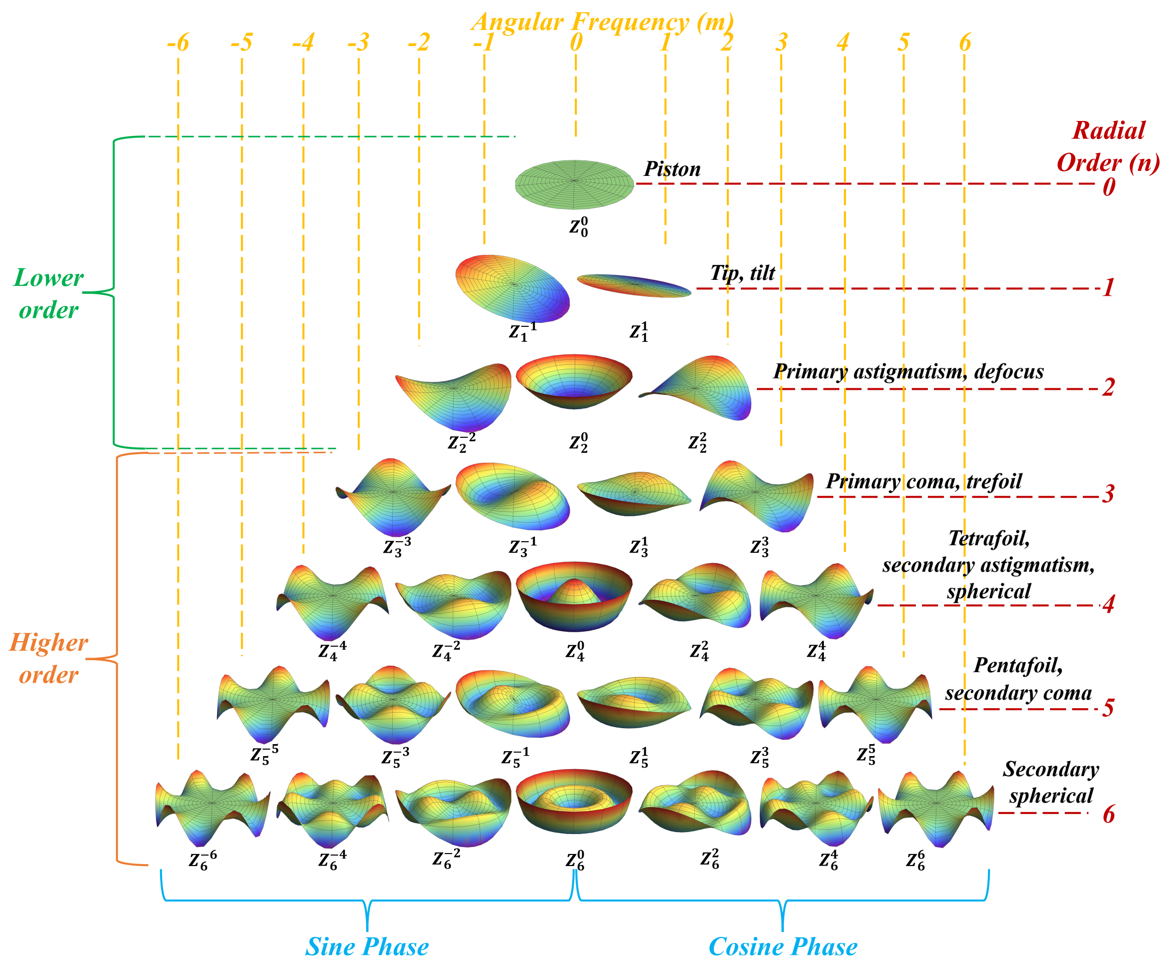

Figure 1.4: The first six order Zernike modes

The Zernike polynomials are expressed in terms of the polar coordinates where, $x = r\ \sin(\phi)$ and $y = r\ \cos(\phi)$. The Zernike polynomials can be either even or odd based on their angular order m. The even Zernike polynomials are given by

$$Z_n^m = (\rho, \phi) = R_n^m(\rho)\cos(m\,\phi) \quad \text{for} \quad m \geq 0 \tag{1.1}$$

and the odd Zernike polynomials are given by

$$Z_n^m = (\rho, \phi) = R_n^m(\rho)\sin(m\,\phi) \quad \text{for} \quad m < 0 \tag{1.2}$$

where ϕ is the azimuthal angle, ρ is the radial distance that is limited to the unit disk ($0 \leq r \leq 1$), and $R_n^m(\rho)$ is the radial function expressed as

$$R_n^m(\rho) = \sum_{k=0}^{\frac{n-m}{2}} \frac{(-1)^k\,(n-k)!}{k!\,(\frac{n+m}{2}-k)!\,(\frac{n-m}{2}-k)!}\,\rho^{n-2\,k} \tag{1.3}$$

To define the magnitude of a given mode or an aberration, the Zernike coefficients, z_n^m, are used. They are obtained by taking the root mean square (RMS) of normalized Zernike expansion, N_n^m. The normalization term is calculated by satisfying the condition of $R_n^{\pm\,m}(1) = 1$ for each n and m values , and it is evaluated as follows:

$$N_n^m = \left(\frac{2(n+1)}{1+\delta_{m0}}\right)^{\frac{1}{2}} \tag{1.4}$$

where δ_{m0} is Kronecker delta function ($\delta_{m0} = 1$ for $m = 0$, and $\delta_{m0} = 0$ for $m \neq 0$). z_n^m is a metric that quantify aberrations. Higher values of z_n^m indicate low optical performance due to greater wavefront error whereas lower values indicate high optical performance with less wavefront error [11, 15, 19, 20], .

The Zernike polynomials are robust to model the wavefronts with lower order aberrations [16]. The wavefront distortions in circular lenses and mirrors are commonly defined and quantified by Zernike polynomials. Especially Zernike coefficients are used in AO to manipulate and characterize the surface deformation of adaptive element [2, 18]. To illustrate the representation of visual aberrations by Zernike polynomials, the first 5 order Zernike modes and corresponding visual aberrations are demonstrated in the Figure 1.5. However, the Zernike polynomials may not be the best choice to represent highly aberrated systems. For instance, the impact of atmospheric distortions in astronomy or manufacturing defects in the fabrication of optical components may not be modelled precisely with using Zernike polynomials [15].

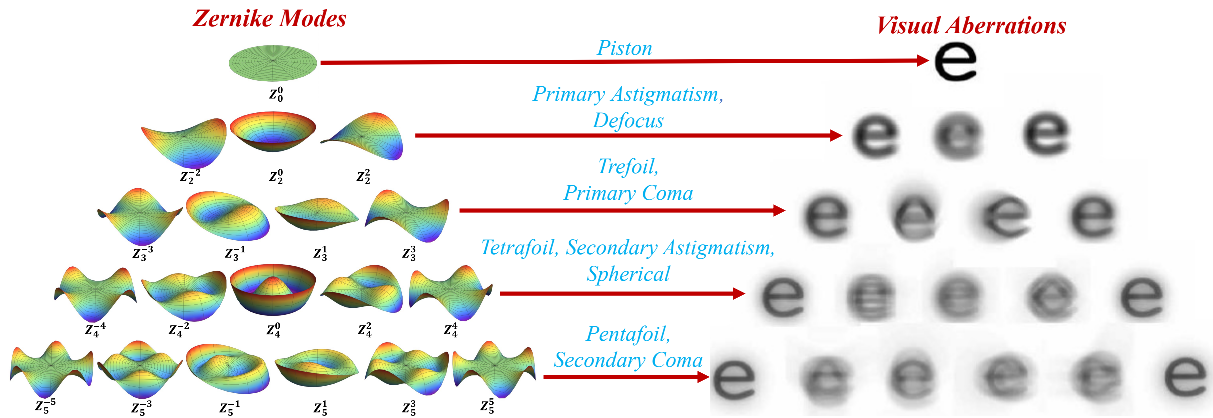

Figure 1.5: The first five order Zernike modes and corresponding visual aberrations

1.1.2 Adaptive Optics

Adaptive optics (AO) is a technology that has been used to measure and correct aberrations dynamically [21]. It was proposed for the first time by H. W. Babcock in 1953 to compensate atmospheric distortions in telescopes. Later on, it was adopted into military applications, ophthalmology, and microscopy. The principle of AO is based upon the use of optical phase conjugation methodology, Figure 1.6. In this technique, the idea is eliminating the wavefront aberrations induced from a forward propagating phase by introducing a backward propagating phase with respect to forward propagating phase. It proposes a reverse propagation methodology where the absolute value of the amplitude is retained as it is, but the direction is inverted. Although phase conjugation helps to compensate aberrations, there is no way to correct all aberrations in a highly aberrated systems with using this technique [22, 23, 24].

AO technology consists of three main process: aberration measurements, compensation of aberrations, and a control systems to track the aberrations over the time [22]. Aberrations can be measured using a wavefront sensor. The most common wavefront sensor is the Shack-Hartman wavefront sensor (SHWS). It comprises of an array of microlenses, and a camera. The incident light passes through the microlenses, and project a focal spot into the camera. The positions of each focal point form the wavefront [25]. Alternatively, interferometry is also used to measure aberrations. In this method, refractive index changes and irregularities across the wavefront are measured by transforming phase variations of distortions to intensity variations of interference fringes [26].

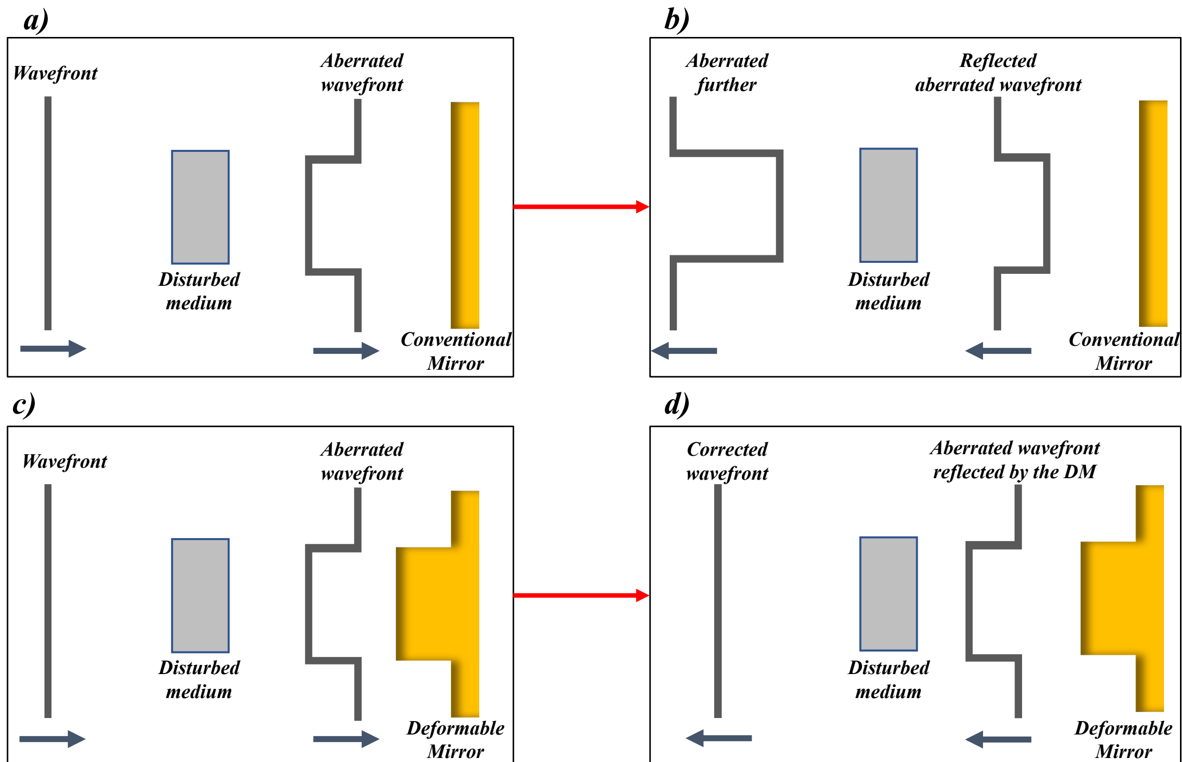

Figure 1.6: Optical phase conjugation principle, a) A wavefront passed through disturbed medium, and it is aberrated. b) The conventional mirror reflected the aberrated wavefront, and it is aberrated once more when passing through disturbed medium. c) An aberrated wavefront is moving towards the DM. d) The reflected aberrated wavefront keeps its shape due to the DM, and when it passes through disturbed medium again, it has become corrected.

Adaptive elements are used to correct aberrations. The most common types are the liquid crystal spatial light modulators (SLMs) and DMs. SLMs are preferred due to its easy use and high resolution. However, their modulation rate is limited in hertz. DMs are the most common type of aberration correction elements in AO because of their low-cost, high optical performance, and fast modulation. The surfaces of DMs are made of highly reflected material which enable to operate independently from polarization and wavelength [13, 27]. Detailed information about DMs will be given in next section.

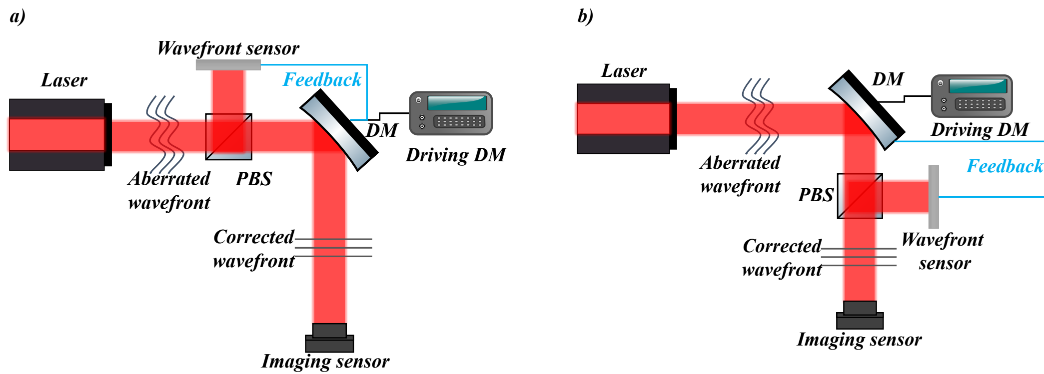

Figure 1.7: a) Open loop AO. b) Closed loop AO.

The control configuration of AO systems can be either open loop or closed loop. In open loop operation, wavefront sensor is used to measure the aberrated wavefront. It is a simple configuration, and commonly used to analyse the influence of aberrations in optical systems. Closed loop operation is more advanced control system where the wavefront sensor measures the distortions in the corrected wavefront, and provides feedback to control DM surface continuously [9, 28]. Figure 1.7 shows both control configurations systems used in AO.

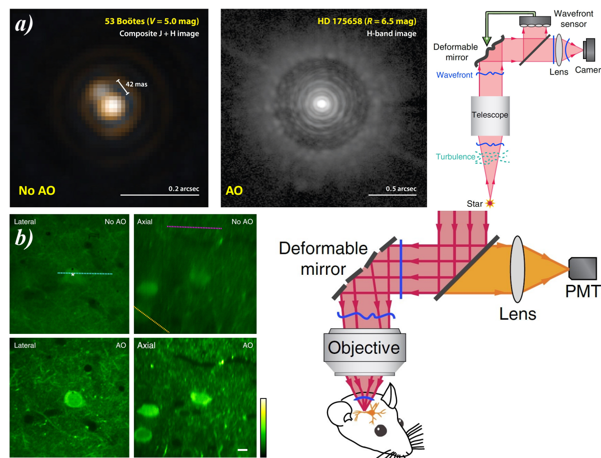

Figure 1.8: AO in a) astronomy [29], images of the double star 53 Bootes using Large Binocular Telescope without AO and with AO. Copyrights© 2012. Annual Reviews. b) Microscopy [30], dentritic spines in mouse brains along the lateral and axial directions imaged without AO and with AO. Copyrights© 2017. Nature Methods.

AO is commonly integrated into optical systems in astronomy [29], microscopy [9, 13, 18], ophthalmoscopy [31, 32], OCT [33], and laser machining [34] to obtain high resolution and high contrast images by compensating wavefront aberrations. Implementation of AO in these disciplines, and resolution improvements are shown in the Figure 1.8 and Figure 1.9.

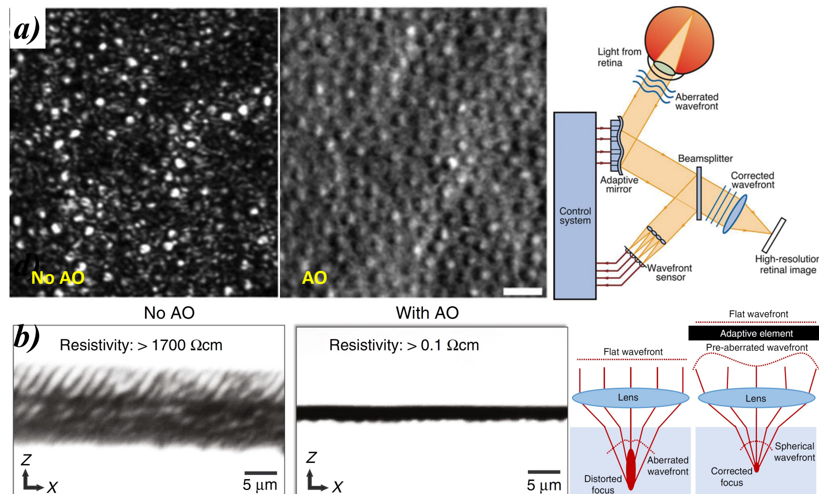

Figure 1.9: AO in a) ophthalmoscopy [35], images of the human photorecetotors of the left eye, and d) laser machining [27], images of graphitic wires beneath the surface of diamond using an ultrafast laser without AO and with AO. Copyrights© 2019. Springer Nature.

1.1.3 Deformable Mirrors

DMs have been developed as wavefront correction and beam shaping components to be used in AO. The aim is compensation of aberrations by deforming the mirror surface locally, and introducing a phase change across the DM profile with respect to aberrations [9, 36]. The DM technology was discovered in 1970s for the use of military driven astronomical researches in the United States [37]. Over the last 50 years, many DMs have been designed to advance the technology. Different types of categorization can be made to classify the DM designs. The most common one is based on surface geometry: segmented or continuous. Additionally, categorization of the DMs may depend on the actuation mechanisms or the geometric arrangement of the actuators [38]. In this subsection, the improvement of the DM technology from conventional DMs to MEMS DMs will be examined, then a brief information about the DM classifications will be given. The diagram of historical developments of DM technology is illustrated in the Figure 1.10.

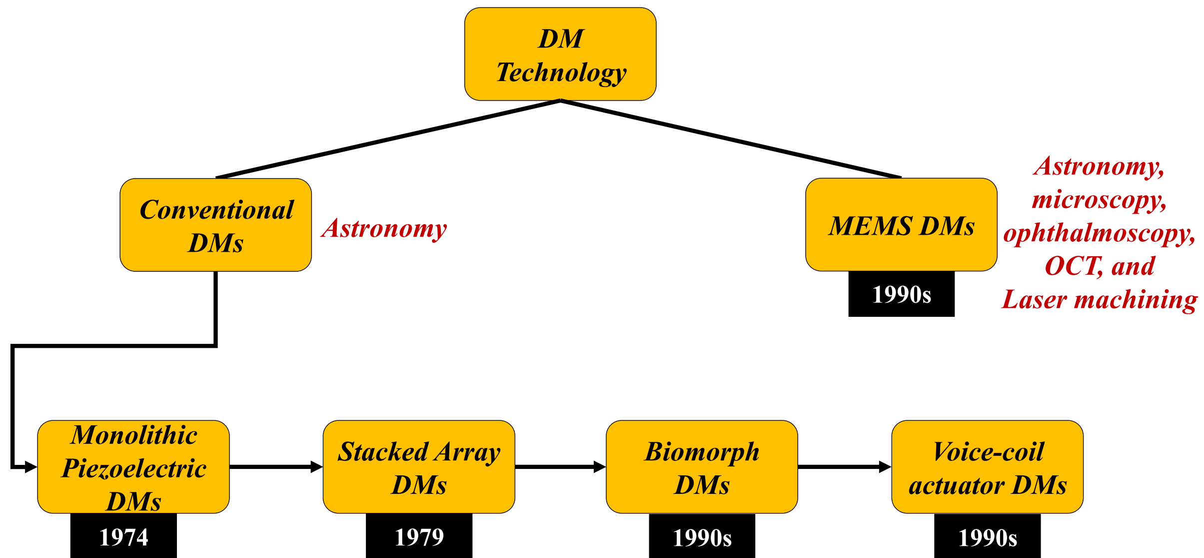

Figure 1.10: Historical developments of the DM technology

1.1.3.1 Conventional DMs

In 1974, monolithic piezoelectric DMs was introduced as a first type of DM to improve the resolution of telescopes [39]. A solid block of lead zirconate titanate (PZT) is used in a monolithic structure as an actuator to deform mirror surface. The device is tremendously stable with high actuator density, but it is not sensitive. In order to achieve ± 1.0 μm surface displacement, ± 3.0 kV is required. Besides, the device has large space occupancy, and high fabrication cost.

Stacked array DMs, Figure 1.11, were developed in 1979 to improve sensitivity by using piezoelectric or electrostrictive actuators made of stacked PZT plates or disks [37, 40]. Stacked array DMs can realize ± 5.0 μm displacements at ± 400 V control voltage. The first eigenfrequency of this mirror appears above 10 kHz. Lead magnesium niobate (PMN) piezoelectric ceramics are also used to fabricate stacked array DMs to reduce the power requirement and temperature sensitivity. In general, stacked array DMs are stiff and provides large stroke with high accuracy. However, their manufacturing process requires high costs due to their structural complexity. High voltages are used to drive stacked array DMs, and they occupy large space because of their bulky structure.

Figure 1.11: Stacked array DM [29]. Copyrights© 2012. Annual Reviews.

Biomorph DMs were developed in 1990s to be used in medium and large size telescopes [37, 40]. The deformation across the mirrors surface is obtained by transverse piezoelectric effect created by two disks of polarized PZT constructed in a sandwich structure. The mirror can realize a stroke which has 14 m radius of curvature along 60 mm pupil diameter biomorph by applying an approximate control voltage of $\pm$400 V. The first resonant frequency is around 1 kHz. Biomorph DMs have very small temperature dependence due to its symmetrical structure, and provides large strokes with high accuracy. Their fabrication process is simpler than stacked array DMs. However, they require high driving voltages, occupy large space, and have low resonant frequencies.

One of the latest development in conventional DMs is the invention of voice-coil based contactless adaptive mirrors in 1990s [41]. It comprises an array of voice-coil actuators, and a continuous shell which floating on an electromagnetic field. The deformation across the DM surface is controlled locally by manipulating the electromagnetic field using voice-coil actuators. The DM can realize approximately 50 µm stroke. The required power consumption for 8 m class telescopes is about 1500-2500 W which brings a necessity of using coolant equipment. This DM technology offers relatively large strokes as compared to other conventional DMs, but the fabrication process is long, complex, risky and very expensive.

The conventional DMs are designed for astronomical observations. Piezoelectric and electromagnetic actuation mechanisms are often used to deform mirror surface. Their large stroke, high accuracy, and fast response time make them attractive correction elements for AO. However, they are bulky, and require high operational voltages associated with complicated circuits. In addition, their manufacturing process are complex and expensive.

1.1.3.2 MEMS DMs

The development of microfabrication proposed MEMS DMs to be used for AO in 1990s [37]. The MEMS technology promises low power consumption, high performance, and miniaturized structures. It broadened the field of AO from astronomy to microscopy, ophthalmology, OCT, and laser machining [9, 29, 31, 36, 42]. Piezoelectric, electrostatic, electrothermal, and electromagnetic actuation mechanisms are mainly used to deform the DM surface [43]. MEMS technology allows to use smaller optics with high performance by reducing the size of actuator spacing from ∼5-7 mm (for stacked array DMs) to ∼300-400 µm. The cost of manufacturing process is also lowered from ∼ $1000 per actuator (conventional DMs) to ∼ $100 per actuator. Low fabrication costs and miniaturized structures makes easy to manufacture large arrays of actuators to reach high resolutions. Besides, it allows to reach relatively high frequencies as compared to conventional DMs, and enables to realize rapid aberration correction for high speed applications [44]. A variety of MEMS DMs have been designed over the last several decades to improve state-of-the-art, and to obtain high resolution imaging. These designs can be categorized into two groups based on their mirror structure: segmented or continuous, Figure 1.12.

Figure 1.12: a) Segmented DM, b) Continuous DM [42]. Copyrights© 2011. Springer Nature.

1.1.3.2.1 Segmented MEMS DMs

An electrostatically actuated MEMS segmented DM, Figure 1.13, was developed to be used for an astronomical observation duty [45]. The DM consists of 329 hexagonal mirror segments, and each segment has 600 µm vertex to vertex distance, and 15 µm thickness. One segment can realize a 1 µm piston stroke when they are tilted to an inclination of 3 mrad by applying an approximately 150 V. There are three rectangular actuators underneath each segment to create electrostatic field. The final structure has an aperture of 9.5 mm to 12 mm. Later on, the design of this DM was improved and manufactured with 37, 169, and 337 segments by Boston Micromachines Corporation (BMC) [46]. The vertex to vertex distance of each segment is increased to 750 µm for these DMs, and the maximum stroke is also improved to 3.5 µm when the mirror has ± 8 mrad tilt angle.

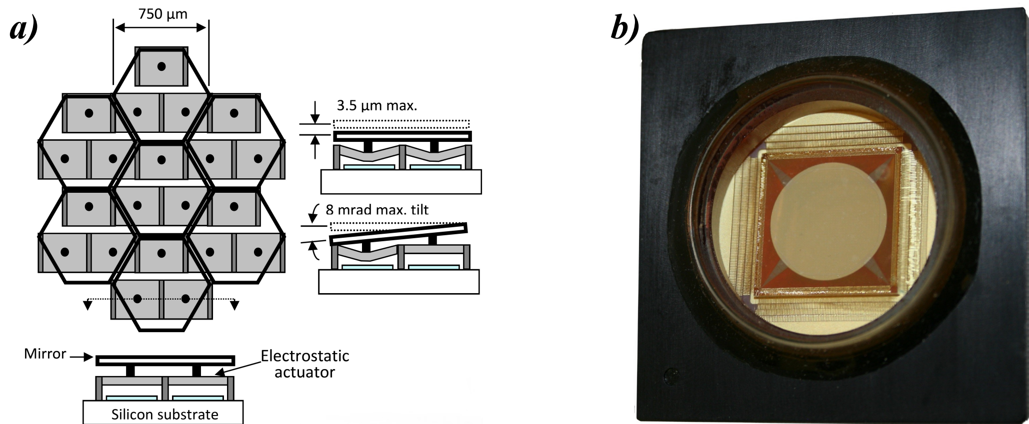

Figure 1.13: a) Schematic of the DM [46], b) Actual device [44].

Iris AO, Inc. (Berkeley, CA) was developed an electrostatic MEMS segmented mirror [47], Figure 1.14. The DM has 37 hexagonal segments which can have 7.5 µm stroke when 125 V is applied to the electrodes. Each segment has 700 µm vertex to vertex distance and 20 µm thickness. There are three diamond-shaped electrodes underneath each segment to create electrostatic field. Applying same voltage to the all electrodes generates piston motion along the mirror segment surface whereas applying different voltages to the electrodes generates tip-tilt motion. The initial air gap is 36 µm. The optical aperture of the DM is 3.5 mm. The design of this DM was changed to scale up larger segmented DM arrays by increasing the segment number to 163 [48]. This DM has 7 µm maximum stroke, and maximum tilt angle of ±5.6 mrad.

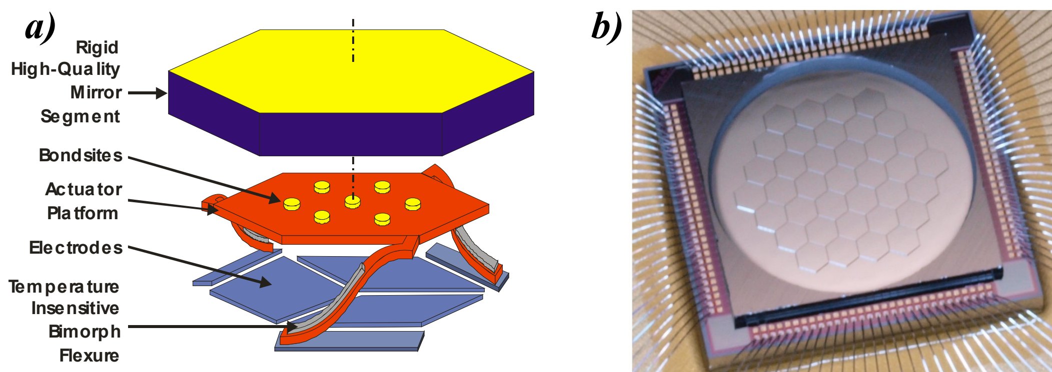

Figure 1.14: a) Schematic of the one segment, b) Actual device [49].

Segmented DMs are preferred due to some of the unique advantages that they offer for AO applications; They do not exhibit cross-coupling between actuators and provide easy controlled adaptive optics system as compared to continuous DMs [36]. The deformation of each segment is provided by the corresponding actuators where zonal influence functions are used to control the drive signal of each actuator, then the combination of each function creates a deformed surface with respect to the measured aberration. Since the segmented DMs consist of independent actuators and mirrors, the structure can easily scale up by adding more elements. The aperture size of the final structure is also adjustable by using tip/tilt actuators to deflect some of the regions across the DM surface. This ability can be used to change shape of the surface or reduce the aperture size. Furthermore, segmented DMs can be used to increase optical efficiency for specific applications such as two-photon microscopy or autofluorescence microscopy by using different coatings along the reflected surface of the independent segments [50]. However, segmented DMs have gaps between each segment, and these gaps can create undesirable diffraction by scattering the incident photons, thereby decreasing the optical efficiency. This is the main disadvantages of segmented DMs. Moreover, segmented DMs does not show any cost or performance benefit as compared to continuous DMs.

1.1.3.2.2 Continuous MEMS DMs

A continuous MEMS DM, Figure 1.15, was designed and fabricated by Boston University and BMC in 2000 [51]. The DM is actuated electrostatically via 140 square electrodes. The mirror surface has 3.3 mm length, 3.3 mm width, and 3 µm thickness. The actuator spacing (pitch) of the DM is 300 µm. The DM consists of 4 main levels: fixed electrodes, moveable diaphragm, attachment posts, and mirror surface. When a voltage is applied to the fixed electrodes, electrostatic field deform the diaphragm, and diaphragm deflects the mirror surface via attachment posts. The maximum stroke provided by the DM is 2 µm, and the maximum drive voltage is 240 V. A 1.5 µm deflection was obtained (the midpoint of the surface) when 220 V is applied to one actuator. The first frequency of the mirror surface is found to be around 6.7 kHz. BMC improved the design of this DM by making a slight changes in the geometrical dimensions, and sell them to their customers. In new versions, there are 137 and 140 actuators, and each one of them has 1.5 µm and 3.5 µm strokes, respectively . The pitch size and the aperture size are also varying for different versions. These continuous MEMS DMs have been used to improve imaging performance in several applications including astronomy, microscopy, ophthalmology, and laser beam shaping.

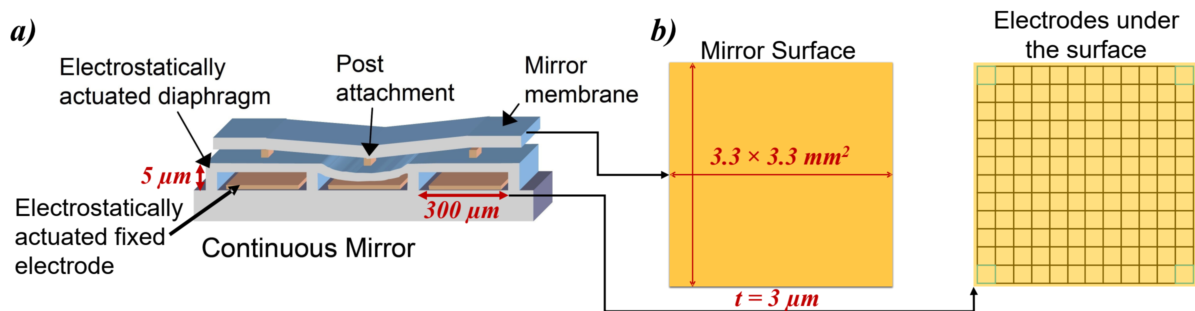

Figure 1.15: a) Schematic cross section of the continuous MEMS DM, b)The surface of the DM, and the 12×12 square electrode grids (w/o corners) [45].

Another continuous MEMS DM was developed by BMC to correct higher order wavefront aberrations in order to eliminate the optical imperfections in an astronomical imaging application [52]. To realize higher performance 4096 actuators are used to generate electrostatic field to deform a continuous facesheet. Each actuator has 400 µm pitch. The DM is able to have 4 µm maximum mechanical stroke. The structure of this DM, and actuation mechanism are similar to the previous continuous MEMS DM mentioned above. The surface is 26.8×26.8 mm^2 square sitting on a 49×49 mm^2 square single crystal silicon die. To prevent squeeze film damping across the such a wide area 6×6 µm^2 holes are etched in the mirror surface. There are 18 holes per single actuator pitch. This MEMS DM is also improved by the BMC, and have been sold and used in different astronomical imaging applications.

Continuous DMs exhibit almost zero diffraction due to continuity of the reflected surface, and provide high optical performance for high resolution and high contrast imaging in many applications as compared to segmented DMs. However, stress and strain in the mirror plate cause mechanical coupling between actuators, and complicate the control mechanism. Modal influence functions are used to select required drive voltage for each actuator in order to replicate desired Zernike mode by using Zernike coefficients. Continuous DMs are often preferred to compensate low order wavefront aberrations due to their high optical performance. But correction of higher order aberrations with continuous DMs requires precise control to eliminate inter-actuator coupling.

1.1.3.2.3 Actuation Mechanisms of MEMS DMs

Different transducing mechanisms are used in MEMS DMs to generate driving force that deforms the mirror surface. Electrostatic, piezoelectric, electromagnetic, and electrothermal actuation

mechanisms are mainly used in MEMS DMs. Each actuation mechanism has advantages and disadvantages.

Piezoelectric actuators are widely used in AO due to their ability to generate large force with low voltage, and to provide high resonant frequency. However, they are encumbered with hysteresis issues, and low compatibility to micromachining [53]. A piezoelectric continuous MEMS DM, Figure 1.16, was designed and fabricated [54]. PZT based piezoelectric unimorph membrane microactuators are used to deform mirror surface. The mirror surface consists of a circular plate that has 2.5 mm diameter, and it is supported by 4×4 actuator arrays via posts. The DM can have 5 µm stroke when 50 V is used as an actuation voltage. The resonant frequency of the mirror is 42 kHz. This mirror suffer from the hysteresis due to piezoelectric actuation.

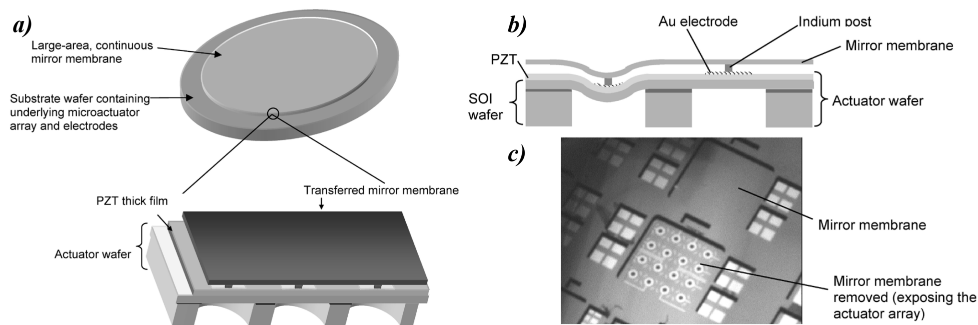

Figure 1.16: a) A schematic of the piezoelectric mirror membrane, and PZT actuators, b) Cross sectional schematic of the piezoelectric DM, c) SEM picture of the DM, and electrode arrays [54]. Copyrights© 2006. IEEE.

Another piezoelectric MEMS DM was designed to be used as varifocal mirror for high-speed focus scanning applications, Figure 1.17 [55]. It has a diameter of 2.6 mm, and actuated by 4 concentric electrodes. Although the DM can modulate with high frequencies (90 kHz) during the defocus mode oscillation, it shows typical response of hysteresis behaviour. The DM is able to replicate only circumferential modes, and different electrode configurations are required for the correction of circumferential modes.

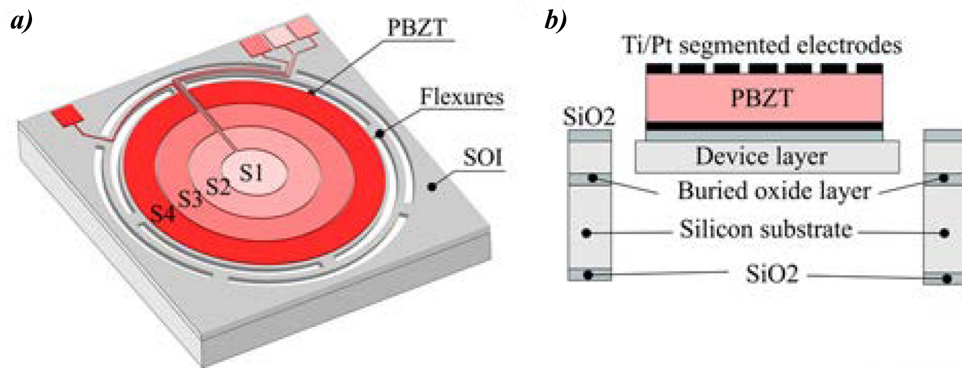

Figure 1.17: a) A schematic of the varifocal piezoelectric MEMS DM, b) Cross sectional schematic of the varifocal piezoelectric MEMS DM [55]. Copyrights© 2021. IEEE.

Electromagnetic and electrothermal actuation mechanisms are also used to drive MEMS DMs. Electromagnetic actuation can produce largest stroke among others, and it can lowered the power consumption. However, a complex structure is needed with multiple coils and permanent magnets to produce abundant energy flux. On the other hand, electrothermal actuation is able to generate high force to reach large stroke, but it is suffered from high power consumption and long response time [56].

1.2 Motivation and Objectives

Extensive research has been conducted to improve the state-of-the-art AO applications. Conventional DMs are developed for the first time to be used in AO for astronomical imaging. Although they compensate wavefront aberrations with high accuracy, provide high stroke, and have fast response time, they have complex working mechanism, high-cost manufacturing process, high power consumption, and large space occupancy. The developments in microfabrication introduced MEMS DMs and advanced the AO. MEMS DMs lowered the overall cost, power consumption, and complexity of fabrication process as compared to the conventional ones. In addition, they expand the scope of AO by miniaturizing the size of the DMs [36, 32, 57].

Electrostatically and piezoelectrically actuated continuous MEMS DMs are mainly used for wavefront correction and focus scanning applications in AO. Electrostatic MEMS DMs use high dense of electrodes to be able to replicate the required Zernike modes for compensation of aberrations. Imitating a Zernike mode needs to control driving voltages for each actuator by using

influence functions. An influence function gives the characteristic shape of the surface deformation when the DM is actuated with a single electrode, and each actuator has an influence function. Realization of a Zernike mode requires to solve a linear system consists of influence functions obtained from each actuator to find zonal (segmented) or modal (continuous) response which corresponds to final deformation across the DM surface. This is accomplished by applying different voltages to each actuator. The control mechanism proposes to minimize the residual error between the measured aberration and required Zernike mode. The operation is repeated until reaching the minimum residual error. Complicated circuit, complex control algorithms, and associated hardware are needed to operate this control system.

Piezoelectric MEMS DMs are used in AO to achieve large stroke, and higher resonant frequencies with low power consumption. They have been widely used in AO for compensation of low order wavefront aberrations, and especially for focus scanning applications. Nevertheless, piezoelectrically actuated DMs are suffered from hysteresis significantly. Hysteresis is a nonlinear effect that reduce the accuracy of the DM response. It causes an error in the state of a DM due to dependence on past inputs, thereby complicating the control mechanism of current input. Moreover, piezoelectric actuators may not be able to correct low and high order aberrations using single actuator arrays. Therefore, designing different actuator arrays are necessary to correct low and high order aberrations, and each design needs different fabrication run. Furthermore, integration of piezoelectric actuators into micromachining is difficult.

Recent developments in imaging systems including microscopy, flight capable exoplanet direct imaging, ophthalmoscopy, OCT, endoscopy, cell phone cameras, tablets, and optical sensors have highlighted the demand for miniaturized, low-cost, easy-driven, rapid, and compact wavefront correction elements to increase image resolution and contrast by compensating optical aberrations in real-time. Although large amount of research has been directed to advance DM technology, the more improvement is needed to satisfy these demands.

In this thesis, we present a novel continuous MEMS DMs that can be a great candidate to meet desired goals, and advance the state-of-the-art. The DM can be integrated into AO systems to compensate high and low order wavefront aberrations, as well as chromatic aberrations instantaneously. REA is proposed as an actuation mechanism to deform the mirror surface. It deploys single sinusoidal waveform to all or selected electrodes to replicate required Zernike mode, thereby eliminating the need for individual actuation electrodes, and reducing the complexity of the control mechanism. REA drives the DM at resonance to benefit dynamic amplification. Thus, it provides larger stroke, minimizes the required electrode counts, and makes able to miniaturize the device architecture. The proposed DM can compensate low and high order aberrations in a single actuator array. The dynamic nature of the actuation allows the correction of aberrations in real-time. Simple device structure enables to reduce fabrication costs, and the complexity of the manufacturing process.

Primary objective of this thesis is investigating the design, fabrication, and characterization of the presented DM, and demonstrating its ability by integrating it into an optical setup as a varifocal mirror to shift a focal point of an incident pulsed laser beam.

The work presented in this thesis has appeared in the following papers:

- A. Kamel, **S. Kocer**, T. Das, L. Mukhangaliyeva, R. Saritas, P. Hajireza, M. Yavuz and E. Abdel- Rahman,"Demonstration of Resonant Adaptive Mirror", *The 21st International Conference on Solid-State Sensors, Actuators and Microsystems (Transducers)*, 2021, pp. 1096-1099. → Published
- **S. Kocer**, L. Mukhangaliyeva, A. Kamel, R. Saritas, T. Das, A. Elhady, K. Bell, A. Gulsaran, M. Kayaharman, P. Hajireza, M. Yavuz and E. Abdel-Rahman,"Resonant Varifocal MEMS Mirror", *The 35th IEEE International Conference on Micro Electro Mechanical Systems (IEEE MEMS)*, 2022. → Accepted
- L. Mukhangaliyeva, **S. Kocer**, M. Boktor, A. Warren, K. Bell, E. Abdel-Rahman and P. Hajireza, "Deformable Mirror-based Focus Control in Photoacoustic Remote Sensing (PARS) Microscopy", *The conference on Adaptive Optics and Wavefront Control for Biological Systems VIII (SPIE BiOS)*, 2022. → Accepted

1.3 The Outline of the Thesis

This thesis is divided into five chapters. The content of each chapter is as follows:

Chapter 1 reviews the literature, explains the research motivations and objectives.

Chapter 2 investigates design and fabrication of the proposed DMs. It also demonstrates the FEM simulation results.

Chapter 3 shows the experimental characterization of the proposed DM.

Chapter 4 exhibits the integration of the proposed DM into an optical setup as a varifocal mirror to demonstrate its focus shifting ability.

Chapter 5 presents the summary of the results, and discusses the future work recommendations.

Chapter 2

Design and Fabrication

In this chapter, the main design criteria and the design of the proposed DM will be described. Then, conducted FEM simulation results, and fabrication steps will be explained.

2.1 Design Criteria

Designing a DM is a process that starts with the identification of the objectives. The defined targets must introduce a novel DM structure that will show high performance to advance the current state-of-the-art AO applications. Then, required system specifications, limitations and materials properties should be described to achieve these objectives. Mathematical tools such as reduced order models or finite element analysis must be used to understand physical mechanism and to find the optimal design of the prototypes that will enable to reach defined objectives. All these design fundamentals should meet with the fabrication constraints. If any one of them does not satisfy the fabrication constraints, it should be updated and adopted to fulfill these requirements [58].

The important system specifications are the size and the geometry of the mirror, the surface topology, the necessary stroke, and the resonance characteristic of the proposed DM. Once these parameters are specified, it is crucial to select proper actuation mechanism, to designate the number of actuators, and to design the distribution of electrodes underneath the mirror surface. Choosing a suitable material for the reflective surface is also critical since that will have huge impact on the DM performance. Three main design criteria are determined to reach defined research objectives that are stated in the previous chapter:

1) The proposed DM must be able to correct low and high order wavefront aberrations. Therefore, the mode shapes of the DM must be able to replicate corresponding Zernike modes, especially biologically relevant modes, namely defocus, astigmatism, coma, trefoil, and tetrafoil.

2) The natural frequencies of the mirror should be greater than the acoustic frequency range $f = 20$ kHz to reduce the impact of external disturbances on the system, and to provide fast modulation.

3) The proposed DM should realize large stroke on the order of 1 μm using a proper actuation mechanism that would minimize the required power consumption. Moreover, the selected actuation mechanism should reduce driving complexity, and provide high performance within a simple architecture. Hence, it reduces the manufacturing costs.

The mirror surface is designed to be circular in order to achieve a precise replication of Zernike modes since these modes are used to describe wavefront aberrations for optical systems with circular pupils. The mirror is supported by beams that are distributed equally and symmetrically around the surface. The support condition is chosen to create sectoral symmetry in the structure, and to realize each Zernike mode smoothly. The number of beams that support the mirror surface are determined by conducting FEM simulations using COMSOL Multiphysics software. It is found that supporting the circular plate with minimum eight beams enables to generate both low and high order Zernike modes.

Electrostatic actuation is used to actuate the DM dynamically. The mirror plate replicates a desired mode by applying a single sinusoidal waveform to all or selected electrodes at the natural frequency of that mode. Exciting the DM at resonance exploits dynamic amplification and increases the stroke. The proposed design can replicate the first six order Zernike modes including biologically relevant modes mentioned above. Driving the electrodes with same voltage eliminates the use of complex control mechanisms and associated hardware. It also cancels the use of influence functions that employed to detect required voltages for each electrode individually.

REA is applied via 49 concentric electrodes. These electrodes are distributed underneath the mirror surface in a circular manner, and they cover almost 97% of the mirror surface area. They are divided into four concentric tiers. One of them is placed at the middle, and the remaining three tiers are encircled the center electrode by constituting sixteen sectors. Due to imposed fabrication constraints, the distance between each electrode and the air gap are set to 40 μm and 20 μm, respectively.

Single crystal silicon is used as a substrate material because of its mechanical stability and its semiconductor properties that allows to integrate it into electronics. Gold is selected as a reflective surface material because of its high reflectivity and endurance.

2.2 Mirror Design

The DM comprised of a circular crystal silicon plate. It has a 1.6 mm diameter and a 10 μm thickness. The plate surface is covered with 75 nm thick gold layer. There are eight equally spaced 100 μm long, 15 μm wide, and 10 μm thick support beams at the circumference of the mirror plate. The DM is actuated electrostatically via 49 electrodes. There is 20 μm air gap between the bottom surface of the plate and top surface of the electrodes. Figure 2.1 demonstrates the dimensions and features of the DM.

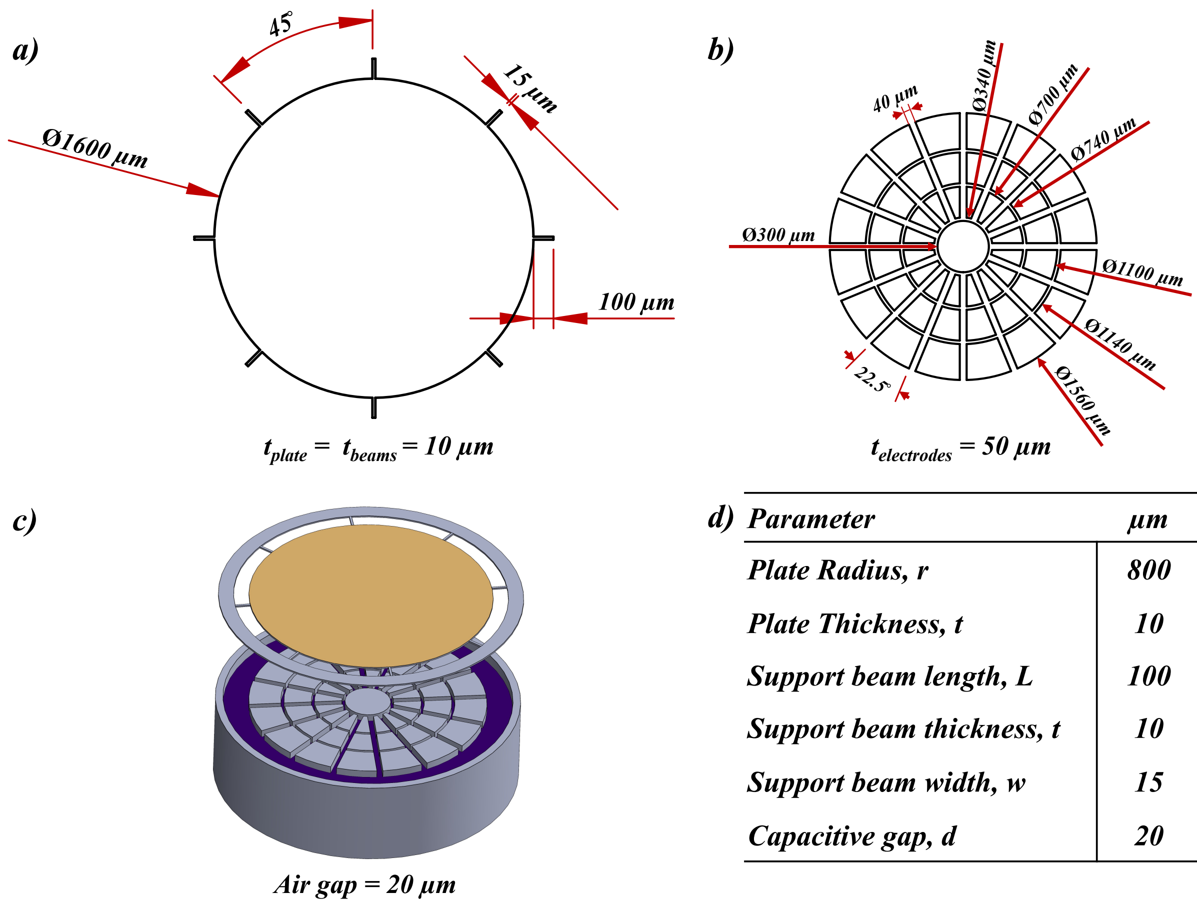

Parameter	μm
Plate Radius, r	800
Plate Thickness, t	10
Support beam length, L	100
Support beam thickness, t	10
Support beam width, w	15
Capacitive gap, d	20

Figure 2.1: a) Dimensions of the mirror plate and surrounding beams, b) Electrodes configuration, c) A schematic of the DM, d) Dimensions of the DM.

Electrostatic forces are generated to deform the mirror surface when a voltage is applied to one or more electrodes while the mirror surface is grounded. The DM approaches a desired Zernike mode via dynamic excitation. A sinusoidal waveform is applied to all or selected electrodes:

$$V(t) = A \sin(2\,\pi\,f\,t) \tag{2.1}$$

where A is the amplitude of the voltage, and f is the excitation frequency. In order to prompt the resonant characteristic, excitation frequency, f, should be set to half of the natural frequency of desired mode $f = f_i/2$ due to quadratic relationship between voltage signal and electrostatic force. Since the DM is operated at resonance, the mirror plate oscillates during the excitation. Therefore, the DM operation depends on the use of pulsed laser beam. The pulse repetition rate (PRR) of the laser should be synchronized with the frequency of the DM oscillations.

Two prototypes were designed for comparison. They have identical dimensions except for the dimensions of the supporting beams. Prototype-1 is supported by the beams with dimensions given above whereas prototype-2 is supported by eight equally spaced 100 µm long, 10 µm wide, and 30 µm thick beams. Figure 2.2 shows these two prototypes. This thesis will investigate only prototype-1. More details about prototype-2 can be found in [59].

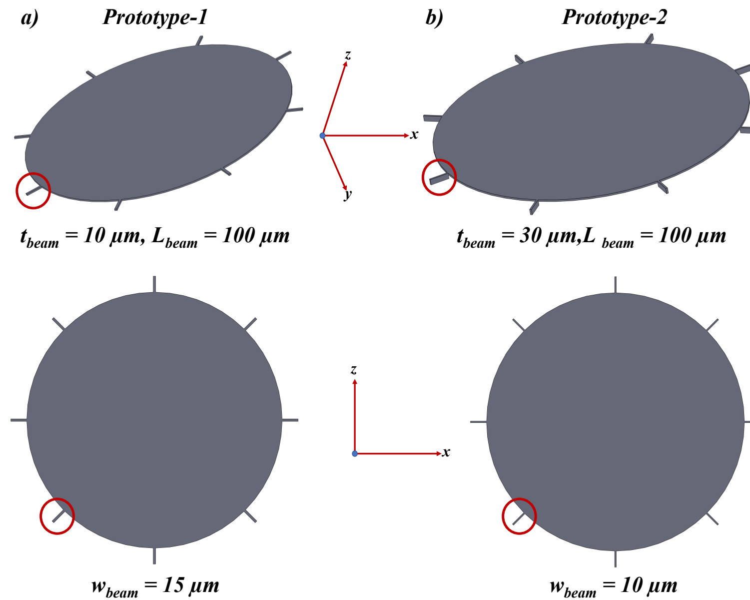

Figure 2.2: a) Dimensions of the mirror plate and surrounding beams, b) Electrodes configuration, c) A schematic of the DM, d) Dimensions of the DM.

2.3 FEM Analysis

2.3.1 Eigenfrequency Analysis

An eigenfrequency study were conducted by using COMSOL Multiphysics software to examine the DM mode shapes and their natural frequencies. The results show that the obtained mode shapes of the DM corresponds defocus (Z_2^0), primary coma ($Z_3^{\pm1}$), astigmatism ($Z_4^{\pm2}$), primary spherical (Z_4^0), trefoil ($Z_3^{\pm3}$), secondary coma ($Z_5^{\pm1}$), tetrafoil ($Z_4^{\pm4}$), and secondary spherical (Z_6^0) modes appear at the frequencies of $f_1 = 23.951$ kHz, $f_2 = 57.07$ kHz, $f_3 = 85.984$ kHz, $f_4 = 105.55$ kHz, $f_5 = 111.9$ kHz, $f_6 = 155.76$ kHz, $f_7 = 208.09$ kHz, and $f_8 = 242.03$ kHz, respectively as shown in the Figure 2.3.

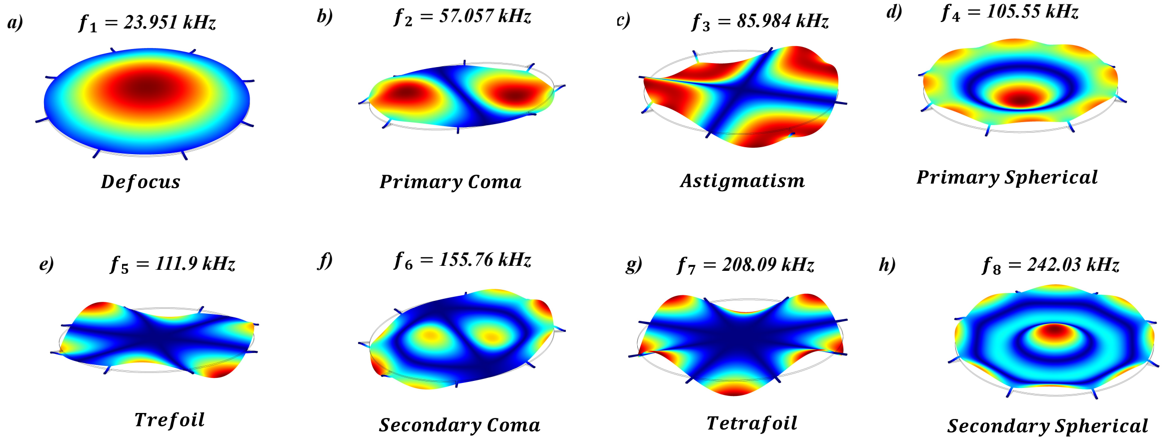

Figure 2.3: Eight mirror plate mode shapes obtained from eigenfrequency analysis in COMSOL: a) Defocus at $f_1 = 23.95$ kHz, b) Primary coma at $f_2 = 57.07$ kHz, c) Astigmatism at $f_3 = 85.98$ kHz, d) Primary spherical at $f_4 = 105.6$ kHz, e) Trefoil at $f_5 = 111.9$ kHz, f) Secondary coma at $f_6 = 155.8$ kHz, g) Tetrafoil at $f_7 = 208.1$ kHz, and h) Secondary spherical at $f_8 = 242.0$ kHz.

2.3.2 Static Analysis

The static response of the DM was also investigated by employing a parametric study in COMSOL Multiphysics using solid mechanics module. The electrostatic force was modelled as a boundary load:

$$F = \frac{\epsilon \, \pi \, r^2 \, V_{\text{dc}}^2}{2 \, (d - w)^2} \tag{2.2}$$

where ϵ is the air permittivity, r is the plate radius, V_{dc} is the applied DC voltage, d is the air gap, and the w is the displacement of the mirror plate on the z-axis. The force is applied to bottom surface of the mirror plate while the end of the supporting beams are fixed. The excitation voltage V_{dc} is swept from zero to until pull-in. The resulting deflection, ω_s-voltage plot of the center point of the bottom surface is illustrated in the Figure 2.4. The pull-in voltage and the corresponding deflection are found to be 363 V and 8.37 µm, respectively.

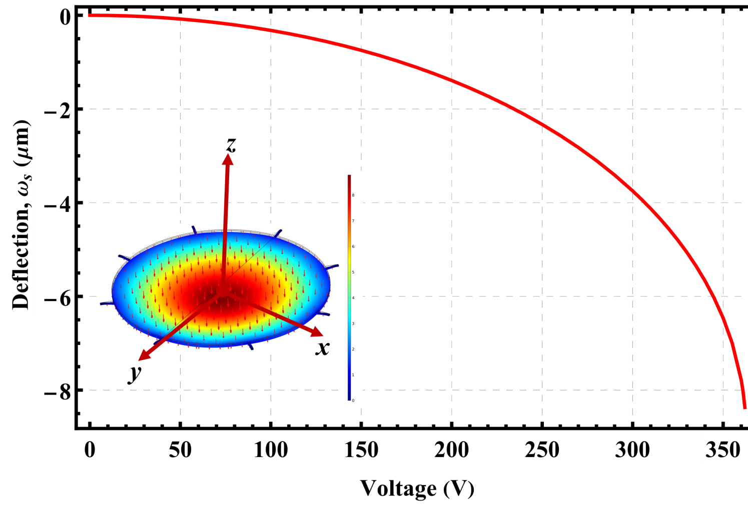

Figure 2.4: Static deflection, w_s of center point of the mirror bottom surface as a function of voltage obtained from the FEM simulation.

2.3.3 Dynamic Analysis

The dynamic response of the DM was also analysed by applying a time-varying excitation forces as a boundary load to the bottom surface of the mirror plate

$$F(t) = \frac{\epsilon\,\pi\,r^2\,(V_{ac}\,\sin(2\,\pi\,f\,t))^2}{2\,(d-w)^2} \tag{2.3}$$

where V_{ac}, the amplitude of the voltage, was set to 150 V. It is assumed that the mirror plate will oscillate at 23.95 kHz which is the oscillation frequency during defocus mode obtained from eigenfrequency analysis. Therefore, the excitation frequency is set to f = 23.95/2 kHz. Rayleigh damping is added the model as

$$[\boldsymbol{C}] = \alpha\,[\boldsymbol{M}] + \beta\,[\boldsymbol{k}] \tag{2.4}$$

where $\boldsymbol{M}$ is the global mass matrix, $\boldsymbol{k}$ is the global stiffness matrix, and α and β are the mass and stiffness proportionality constants. The damping ratio ζ_i for a single mode i can be expressed as

$$\zeta_i = \frac{\alpha}{2\,\omega_i} + \frac{\beta\,\omega_i}{2} = \frac{1}{2\,Q_i} \tag{2.5}$$

The DM is considered as low pass filter. Thus, damping caused by mass is ignored, $\alpha = 0$. The quality factor of the system was set to a low value $Q = 1.5$ due to squeeze film damping [60, 61], and β is found as

$$\beta = \frac{1}{Q\,2\,\pi\,f_s} \tag{2.6}$$

where f_s =2f = 23.95 kHz is the DM oscillation frequency. The time is swept from zero to, 3/f second with 1/f/300 step size. The displacement time-history of the midpoint of the mirror bottom surface was obtained from the simulation, Figure 2.5. It is found that the mirror plate oscillates with an amplitude of 492.5 nm.

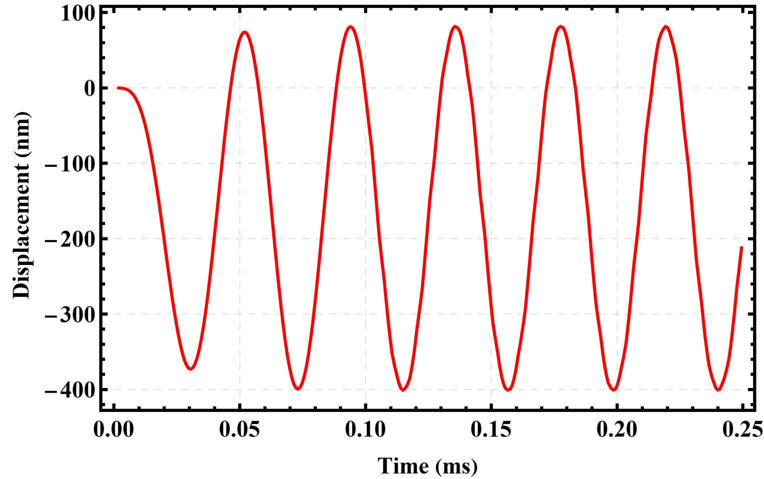

Figure 2.5: Displacement time-history of center point of the mirror bottom surface under a sinusoidal actuation signal obtained from FEM simulation.

2.4 Fabrication

The DM was fabricated using MicraGEM-Si fabrication process at CMC Microsystem Corporation facilities. Two silicon-on-insulator (SOI) wafers of (100) was used. These process includes

a bottom wafer and a top wafer. The material properties of the crystalline silicon layers are listed in the Table 2.1.

Table 2.1: Material properties of the crystalline silicon layers

Material properties	***Value***
Modulus of Elasticity, E, GPa	***129.5***
Density, ρ , kg/m^3	***2320***
Poisson's ratio, ν	***0.28***

The bottom wafer consists of 50 µm thick device layer, 1 µm thick silicon oxide layer, and 500 µm thick handle layer. The top wafer has a 30 µm device layer, a 1 µm silicon oxide layer, and 500 µm handle layer. The fabrication of the DMs consists of six masks Substrate, Trench 1, Trench 2, Y Mask, Metal deposition, and Z Mask. The characteristics of these layers are listed in the Table 2.2, and demonstrated in the Figure 2.6. The masks were designed to fabricate two prototypes in a chip.

Table 2.2: Characteristics of the fabrication masks

Masks	***Description***
Substrate	***Defining the substrate***
Trench 1	***51 µm DRIE etching to device layer of the bottom wafer***
Trench 2	***35 µm DRIE etching to device layer of the bottom wafer***
Y Mask	***20 µm DRIE etching to device layer of the top wafer***
Metal	***75 nm gold depostion on device layer of the top wafer***
Z Mask	***30 µm DRIE etching to device layer of the top wafer***

The fabrication contains 7 steps.

Step 1: Defining Trench 1 and Trench 2 on the bottom wafer.

Step 2: Etching the device layer of top wafer (Y Mask).

Step 3: Bonding bottom wafer to top wafer.

Step 4: Removing the handle layer and silicon oxide layer of the top wafer.

Step 5: Depositing gold on the top wafer.

Step 6: Releasing the pattern by etching (Z Mask)

Step 7: Singulation

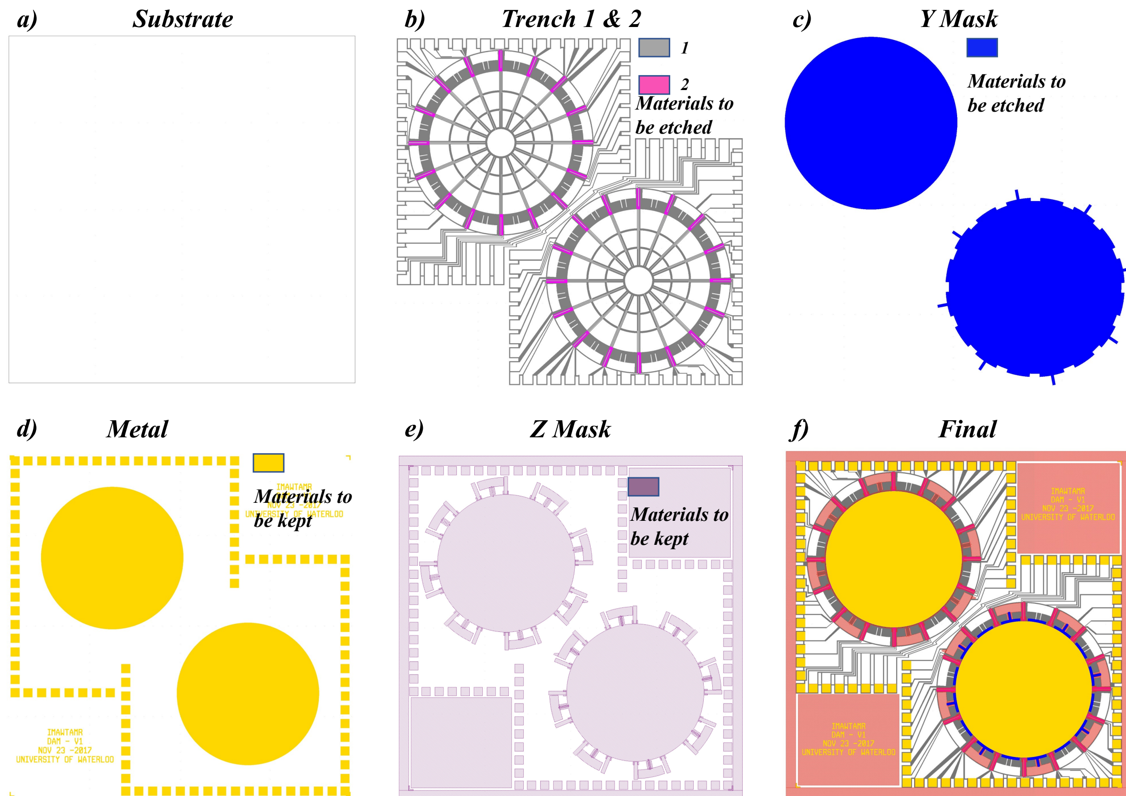

Figure 2.6: a) Substrate, b) Trench 1 and Trench 2, c) Y Mask, d) Metal deposition, e) Z Mask, f) Final layout

Electrodes and their connections are patterned on the device layer of bottom wafer with Trench 1 and Trench 2. These two masks used to etch bottom wafer with deep reactive-ion etching (DRIE). Trench 1 DRIE etched entire 50 μm device layer and 1 μm buried oxide layer to form electrodes. Trench 2 DRIE etched to depth of 35 μm to form connections of the electrodes. Mirror plate, support beams, and bond pads were patterned on the device layer of top wafer by a single DRIE etch to depth of 20 μm using Y Mask. Bottom wafer and top wafer were connected to each other by anodic bonding. Handle layer and buried oxide layer of the top wafer were removed by wet etching. Gold deposited on the mirror surface and bond pads. Finally, the release pattern was defined by a DRIE etching with depth of 30 μm using Z Mask to free the

structure. 2D illustrations of fabrication steps are shown in the Figure 2.7.

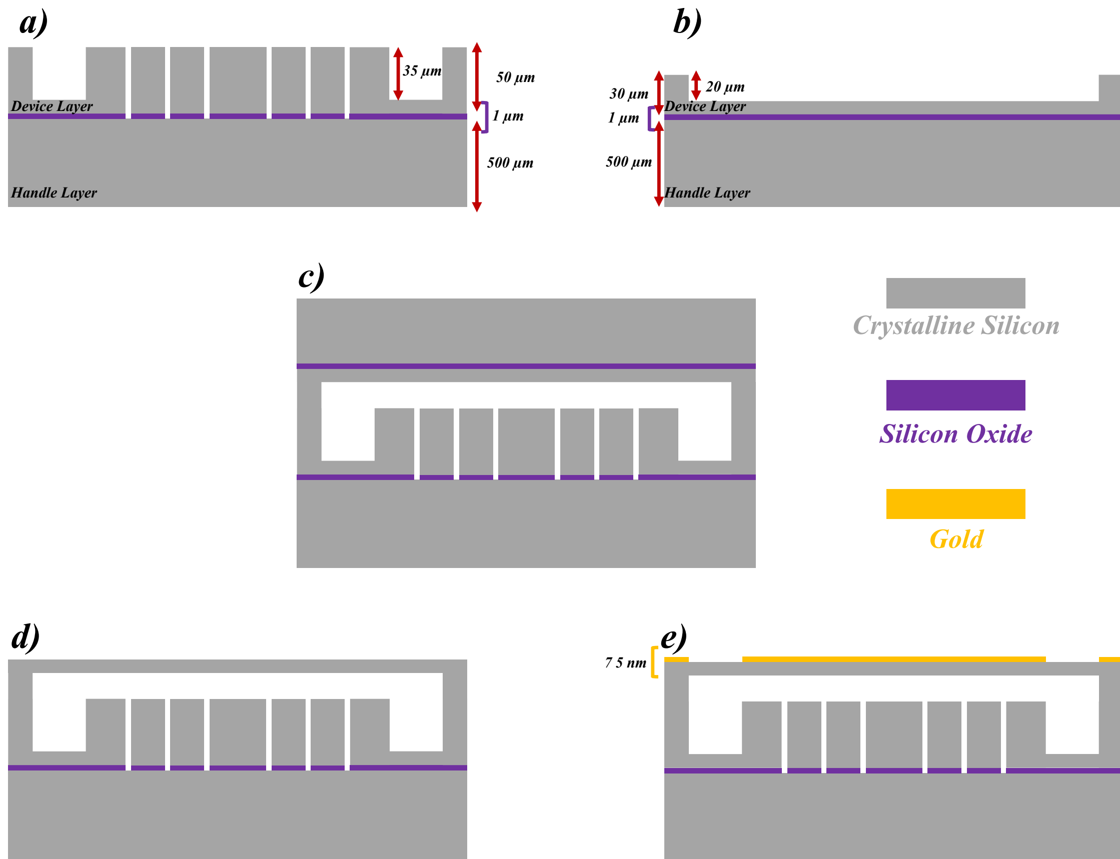

Figure 2.7: a) Patterning electrodes with DRIE etching (Trench 1, 51 µm, and Trench 2, 35 µm, b) Patterning mirror, support beams, and posts wit DRIE etching (Y Mask), c) Anodic bonding, d) Removing handle layer and buried oxide by wet etching on top wafer, e) Gold deposition

2.5 Packaging

The DM chip has 50 bond pads for each prototypes. One of them connect the mirror plates to the ground, and the remaining 49 are connected to the electrodes. Bond pads are sitting on the Metal layer, and they consist of 100 µm × 100 µm square that are placed around the mirror plates in a single row or column. The distance between each pad is 50 µm. The fabricated chips were

wirebonded to an 84 pins grid array (PGA) chip carrier with a cavity size of 11.938 × 11.938 mm. Chip carrier, the backside of it, and a wirebonded chip are shown in the Figure 2.8.

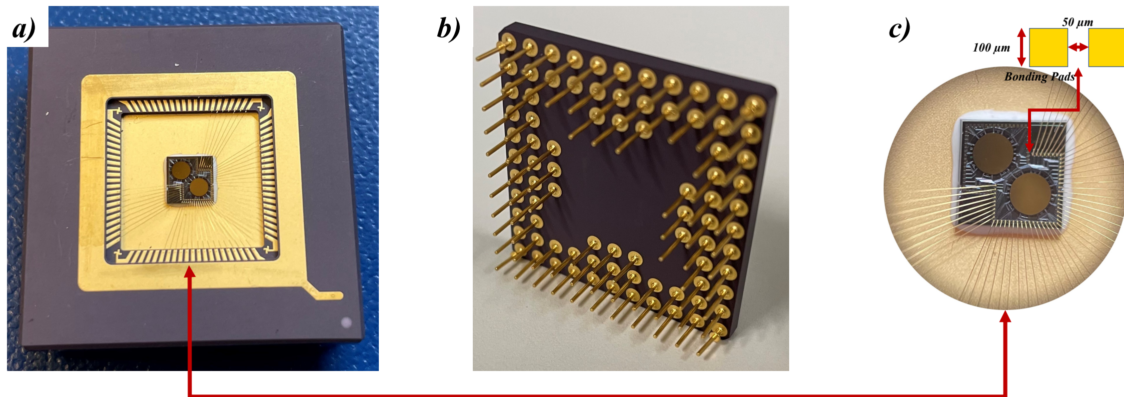

Figure 2.8: a) Chip carrier, b) Backside of the chip carrier, c) Wirebonded chip

In order to drive the DM, a printed circuit board (PCB) was developed that will allow to reach each electrodes individually. A zero insertion force (ZIF) socket consists of 12×12 pin arrays was integrated into the PCB, and 84 pins of the chip carrier was plugged into the socket, Figure 2.9(a). This drive circuit was used during experiments to actuate the DM Figure 2.9(b).

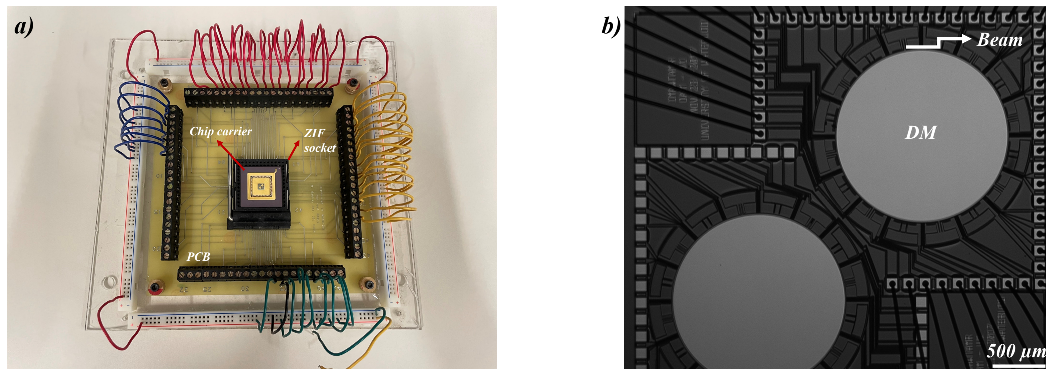

Figure 2.9: a) The PCB used to reach each actuation electrodes individually, b) A microscopic picture of the DM

Chapter 3

Experimental Characterization

In this chapter, experimental characterization of the fabricated DMs are explained. Experimental setup and measured results are demonstrated. The characterization are conducted to investigate: (i) resonant characteristics of the DM, (ii) experimental mode shapes, and (iii) the deformation of mirror plate during defocus mode oscillation.

3.1 Experimental Setup

The DM is actuated using the PCB described above. A function generator supplied the voltage for the excitation signal. The signal was amplified with a gain of 50 using a voltage amplifier. LDV was used to measure the DM response optically, and the signal of the response was observed using an oscilloscope. Figure 3.1 shows a schematic and a picture of the experimental setup.

3.2 Modal Analysis

Modal analysis was conducted to determine natural frequencies of the DM mode shapes. This was carried out by applying an impulse with an amplitude of 75 V, a frequency of 1 kHz, and 0.02 ms pulse width to all actuation electrodes. LDV was used to measure velocity-time history of the mirror plate by focusing the laser spot on the center and on the circumference of the mirror plate to capture axisymmetric modes and circumferential modes, respectively. The time-history of the velocity responses were averaged over a 100 pulses, and are shown in the Figure 3.2.

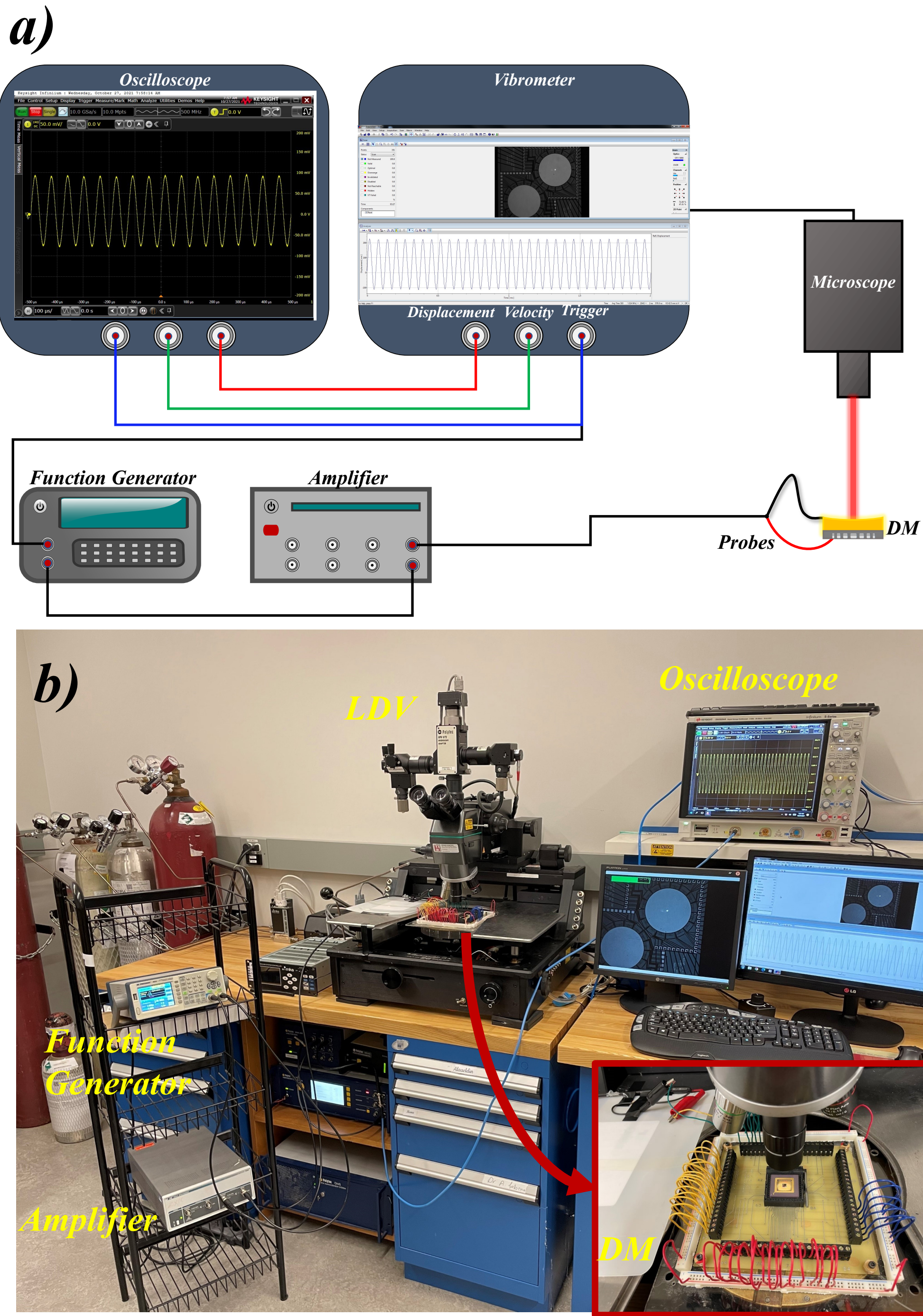

Figure 3.1: a) Schematic of the experimental setup, b) A picture of the experimental setup

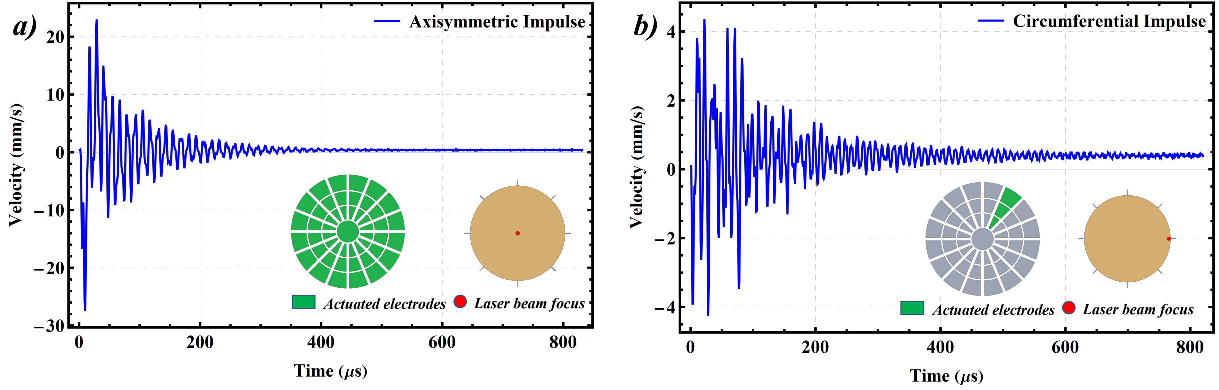

Figure 3.2: Measured responses to the applied impulses, a) Axisymmetric impulse, b) Circumferential impulse. Subsets of the each figure show the actuation scheme, and measurement locations on the mirror plate.

The fast Fourier transform (FFT) was performed to obtain frequency domain velocity responses for the axisymmetric and circumferential impulses. The FFT of the center point velocity results with three peaks corresponding to the axisymmetric modes, namely defocus (Z_2^0), primary spherical (Z_4^0), and secondary spherical (Z_6^0) Zernike modes, appearing at the frequencies of $f_1 = 16$ kHz, $f_2 = 81$ kHz, and $f_3 = 187$ kHz, respectively. On the other hand, the FFT of the perimeter point velocity results with eight peaks corresponding the circumferential modes and the three axisymmetric modes described above. Specifically, the peaks at $f_2 = 43$ kHz, $f_3 =68$ kHz, $f_5 = 87$ kHz, $f_6 = 105$ kHz, and $f_7 = 122$ kHz corresponding to primary coma ($Z_3^{\pm 1}$), astigmatism ($Z_4^{\pm 2}$), trefoil ($Z_3^{\pm 3}$), tetrafoil ($Z_4^{\pm 4}$), and secondary coma ($Z_5^{\pm 1}$) Zernike modes, respectively. Figure 3.3 demonstrates the obtained FFT responses.

The multi-point scanning mode of the LDV was used to capture experimental mode shapes. First, the three axisymmetric mode shapes were realized by applying a harmonic voltage signal with an amplitude of 100 V to the electrodes of the axisymmetric actuation scheme:

$$V(t) = 100 \sin(2\,\pi\,f\,t) \tag{3.1}$$

where the excitation frequency was set to half of the natural frequency of each mode $f = f_i/2$. Then , the circumferential modes were captured by applying the same harmonic voltage, Equation 3.1, described above to the electrodes of the circumferential actuation scheme. Once again the frequency of the signal was set to half of the natural frequency of each mode. Figure 3.4 shows the extracted experimental mode shapes.

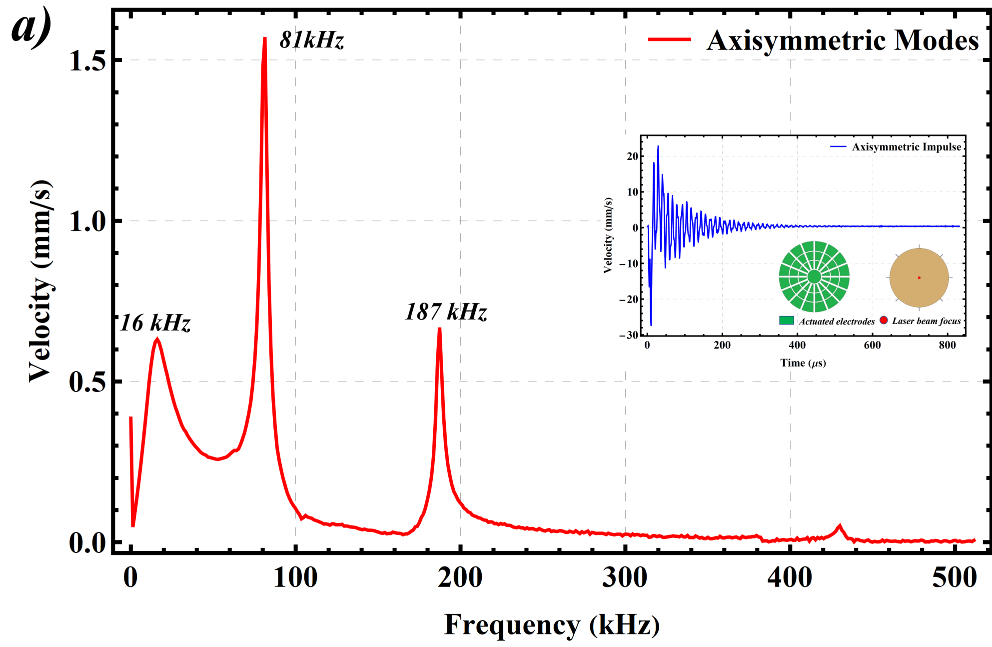

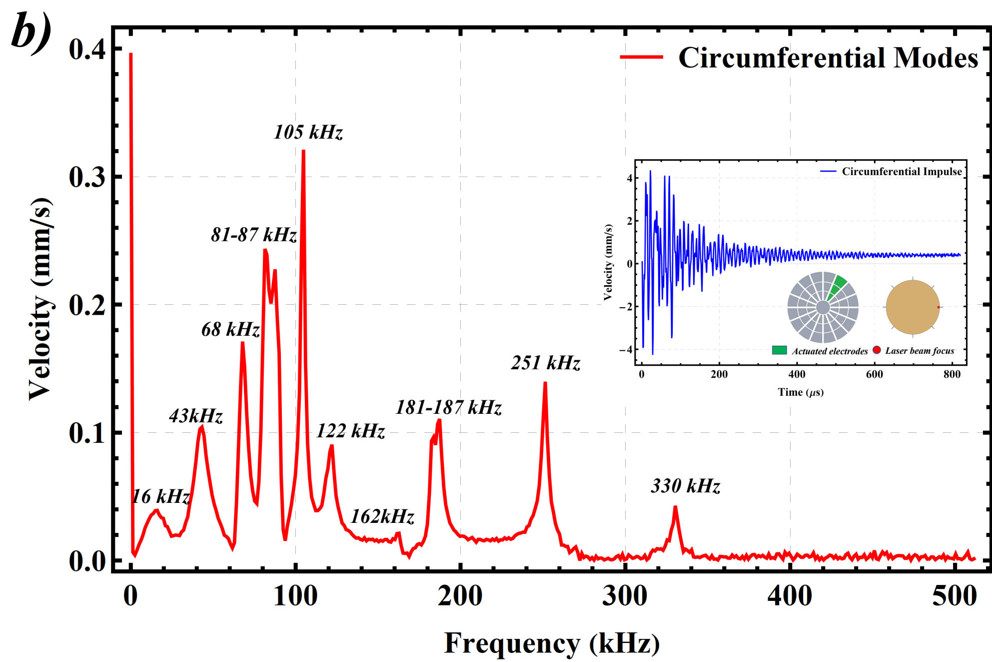

Figure 3.3: a) The frequency-response curve of the DM to a) an axisymmetric impulse, and b) a circumferential impulse

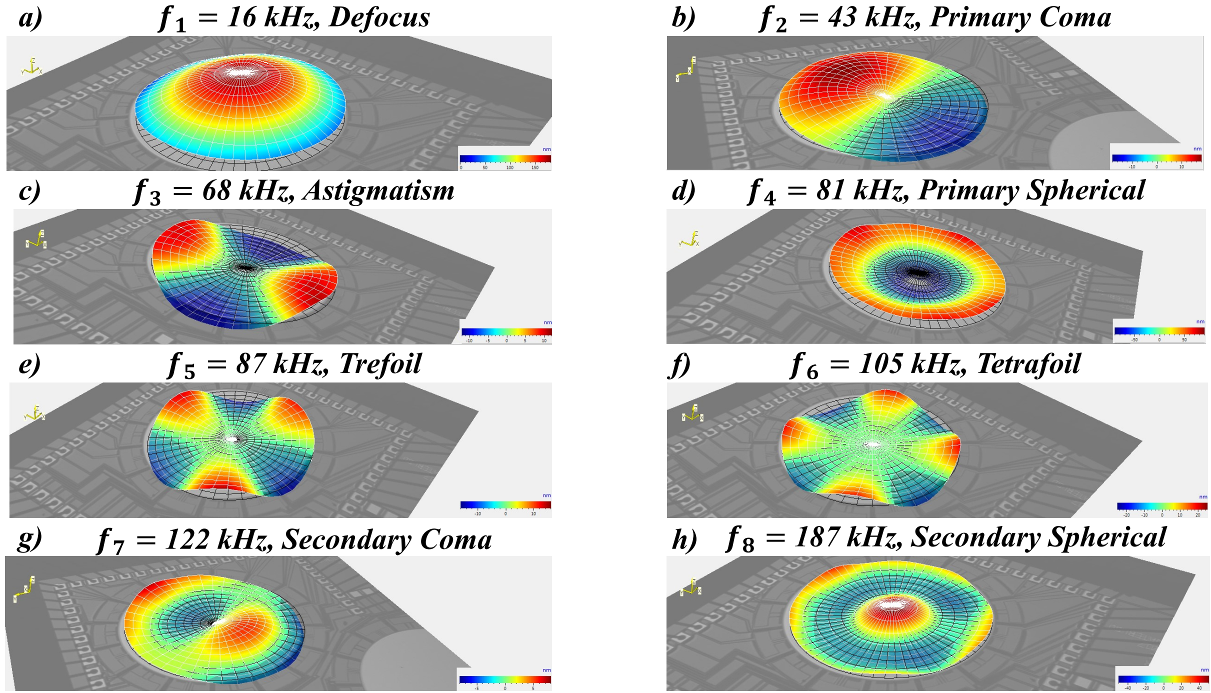

Figure 3.4: Experimental mode shapes obtained by using LDV, a) Defocus mode at $f_1 = 16$ kHz, b) Primary coma at $f_2 = 43$ kHz, c) Astigmatism at $f_3 = 68$ kHz, d) Primary spherical at $f_4 = 81$ kHz, e) Trefoil at $f_5 = 87$ kHz, f) Tetrafoil at $f_6 = 105$ kHz, g) Secondary coma at $f_7 = 122$ kHz, h) Secondary spherical at $f_8 = 187$ kHz.

3.3 Curvature of the DM at Defocus Mode

The first axisymmetric mode of the DM, defocus mode, can be used to change the focal point of a reflected laser beam. Consequently, it can be integrated into various optical systems as a varifocal mirror. To demonstrate this ability of the DM, the evolution of the surface profile while oscillating in this mode was characterized as a function of phase angle ϕ which was considered to be the phase difference between the signal of the defocus mode oscillation and the pulse signal of the incident laser beam. It is assumed that the zero-crossing of the mode corresponds to a flat surface where $\phi = 0°$ or $\phi = 180°$. The DM actuated by applying a harmonic waveform of Equation 3.1 to electrodes of the axisymmetric actuation scheme while the frequency of excitation signal was set to $f_1/2$= 8 kHz. The LDV was used to measure the displacement along the DM diameter at 15 evenly spaced point-grid extending from the tip of one support beam to the

tip of the opposite as illustrated in the Figure 3.5.

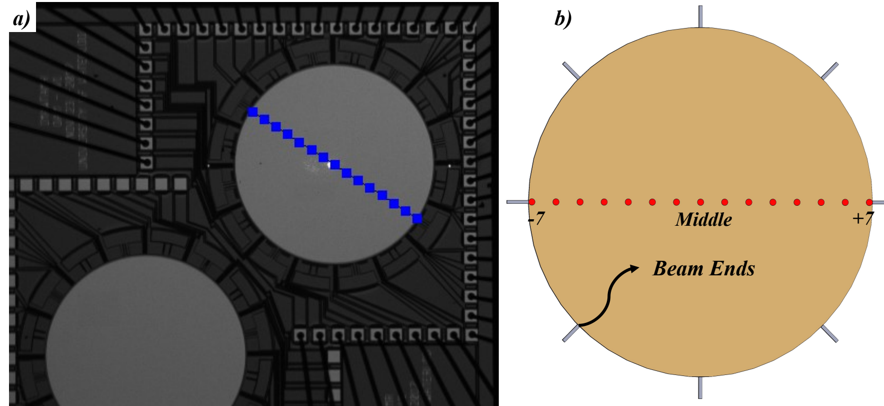

Figure 3.5: a) The point-grid used to measure the DM surface deformation., b) Numbering the grid points

The relative displacements with respect to beam tips were used to measure the mirror surface deformation. First, the equilibrium surface profile of the DM oscillation during the defocus mode is defined. This is the profile where the mirror oscillates around it. It was measured by applying a step voltage with a frequency of 1.024 kHz and amplitude of 70.71 V to the all electrodes. The applied step voltage is equal to the root mean square (RMS) of the harmonic signal Equation 3.1. The LDV was used to measure the displacement at the 15 point-grid. Figure 3.6(a) shows the static displacements at the grid points over the two excitation cycles. The position of each point on the equilibrium surface was recorded when the transients which are excited by the rising edge of the step voltage is settled down.

Next, oscillations of the mirror profile along the same point-grid was measured by applying a sinusoidal waveform as described in the Equation 3.1. Figure 3.6(b) shows the one period of the oscillations under the defined harmonic signal at each point-grid.

Further, the displacement-time history of the DM under this waveform were transformed from time-domain to phase angle domain by expressing one period oscillation, T=62.5 µs, in terms of the phase angle, $\phi_{\text{oscillation}} = [0°, 360°]$. This equivalency assumes that the DM is flat when $\phi_{\text{oscillation}} = 0° = 180° = 360°$. It also assumes that the DM is at the most concave deformation when $\phi_{\text{oscillation}} = 90°$, and at the most convex deformation when $\phi_{\text{oscillation}} = 270°$.

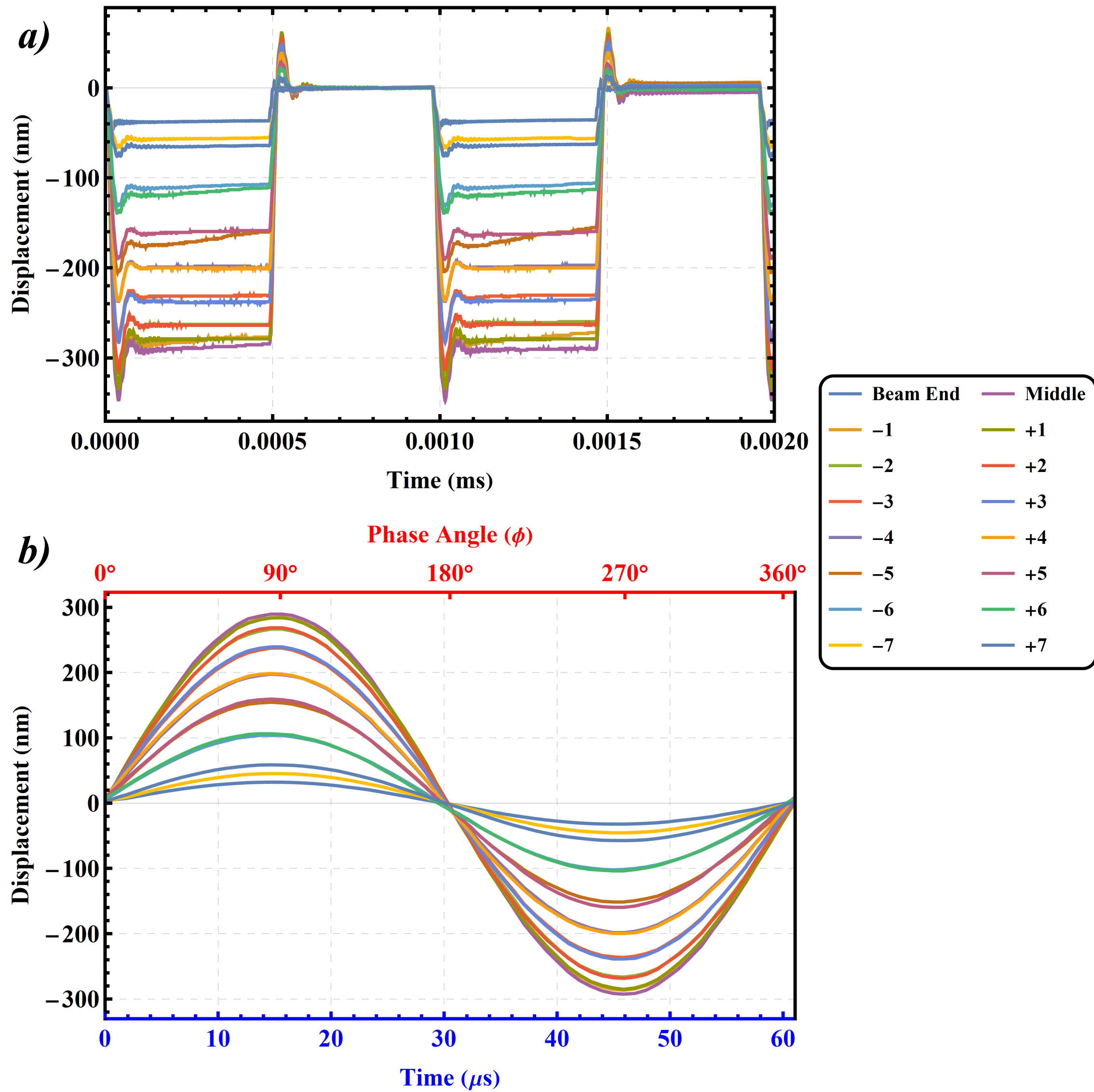

Figure 3.6: a) Static response: The displacement time-history at 15 evenly spaced points under a 70.71 V step voltage, b) Dynamic response: The measured oscillations of the point-grid under a sinusoidal waveform with 100 V amplitude and 8 kHz frequency.

The equivalent phase angle domain is also shown in the Figure 3.6(b) with red colour frame on the top. This plot demonstrates the oscillation of each point-grid around the equilibrium surface profile obtained from the measurements shown in the Figure 3.6(a). Finally, the two sets

of the measurements were combine to calculate the oscillations of each point with respect to equilibrium surface profile.

Using these measurements, the evolution of the mirror surface along the point-grid diameter at 19 different phase angles starting from the $\phi_{\text{oscillation}} = 90°$ to $\phi_{\text{oscillation}} = 270°$ with 10° step size during the oscillation cycle were calculated. To estimate the DM surface at these phase angles, a least square fit function was employed.

$$w^{\phi}(r) = a + b\,r^2 + c\,r^4 \tag{3.2}$$

where a, b, and c are coefficients of the fit function. Figure 3.7 shows the evaluated surface profiles at 19 phase angles during the oscillation cycle. The dashed line represents the equilibrium surface, and the solid lines represent the DM surface at different phase angles

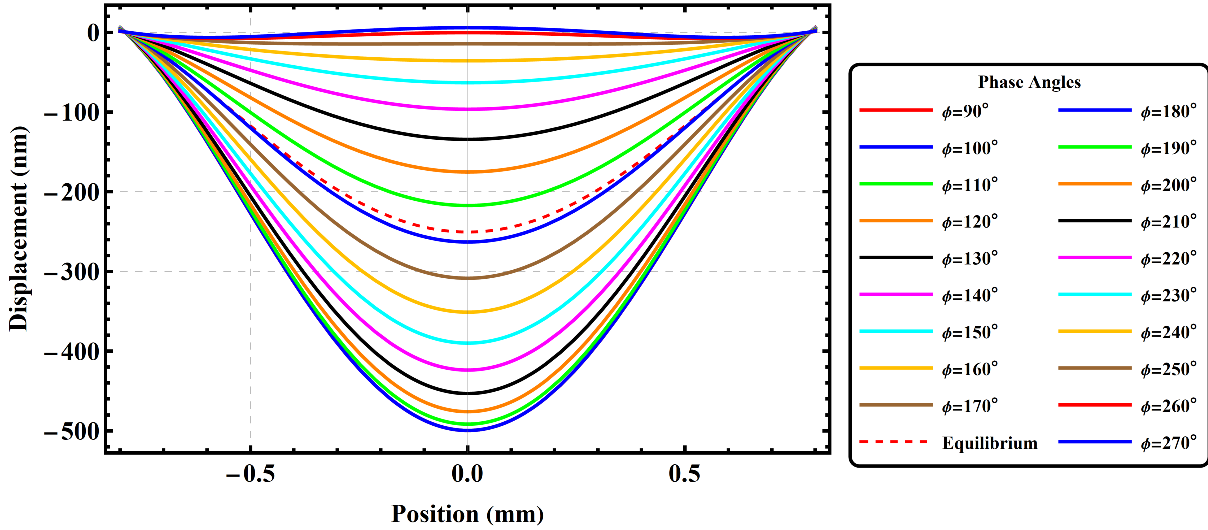

Figure 3.7: The DM surface along the point-grid diameter at 19 oscillation phase angles $\phi_{\text{oscillation}}$.

Then, the radius of curvature for each surface profile was calculated using radius of curvature formula:

$$\rho^{\phi}(r) = \frac{[1 + (\frac{d\,w^{\phi}(r)}{d\,r})^2]^{\frac{3}{2}}}{\frac{d^2 w^{\phi}(r)}{d\,r^2}} \tag{3.3}$$

Table 3.1 lists the phase angle and corresponding radius of curvature at the plate centre $\rho^{\phi}(0)$

Table 3.1: The radius of curvature at the plate centre for a set of seven selected phase angles $\phi_{\text{oscillation}}$.

Phase Angle $\phi^{\circ}_{\text{oscillation}}$	*90°*	*120°*	*150°*	*180°*	*210°*	*240°*	*270°*
Radius of Curvature ρ ***(m)***	*0.39*	*0.41*	*0.5*	*0.74*	*1.15*	*9.0*	*-7.2*

A comparison has been made between the theoretical Zernike defocus mode and the measured defocus mode in order to evaluate the error. The least square fit function described above was used to represent the mirror surface profile when the phase angle $\phi_{\text{oscillation}} = 90°$. The comparison was carried out with the nondimensionalized values. Figure 3.8 shows the comparison.

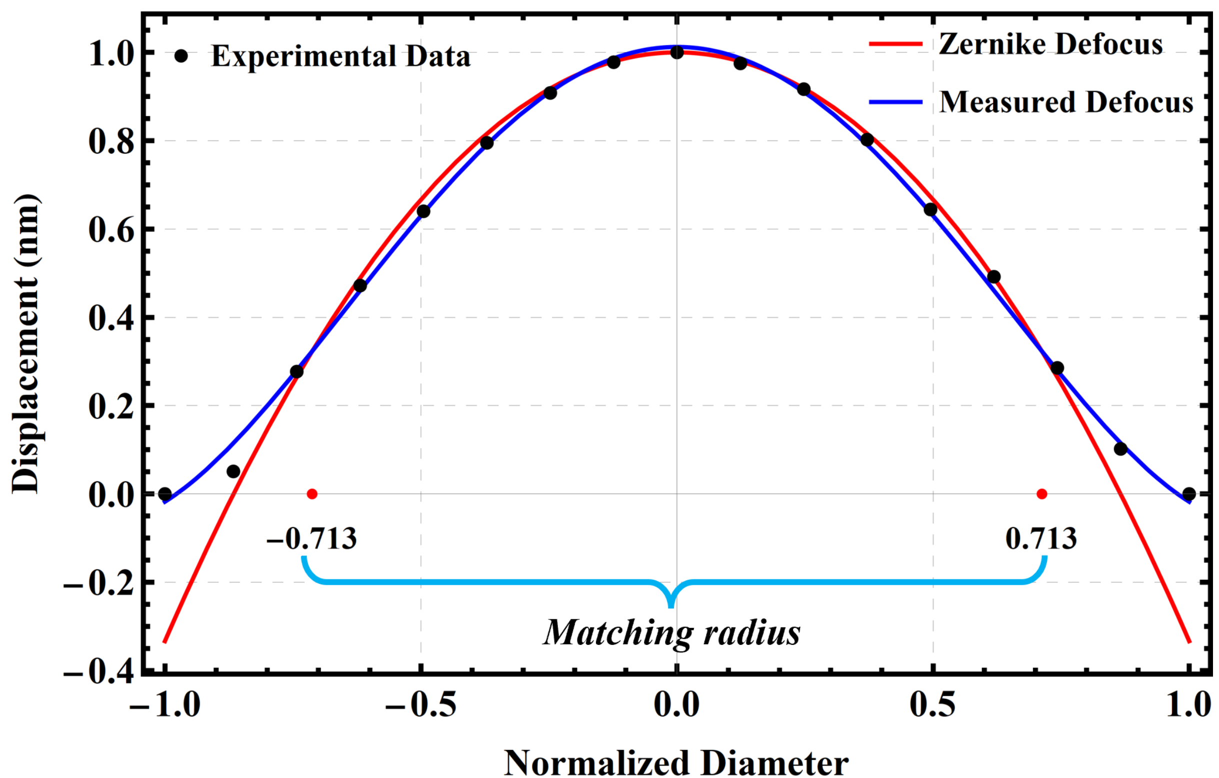

Figure 3.8: A comparison between the measured defocus and Zernike defocus using normalized values

It is found that there is a precise match between the measured defocus and Zernike defocus in the approximately 71% of the radial area. The RMS error is also calculated to be less than 0.05 for a diameter of 1.1 mm, Figure 3.9.

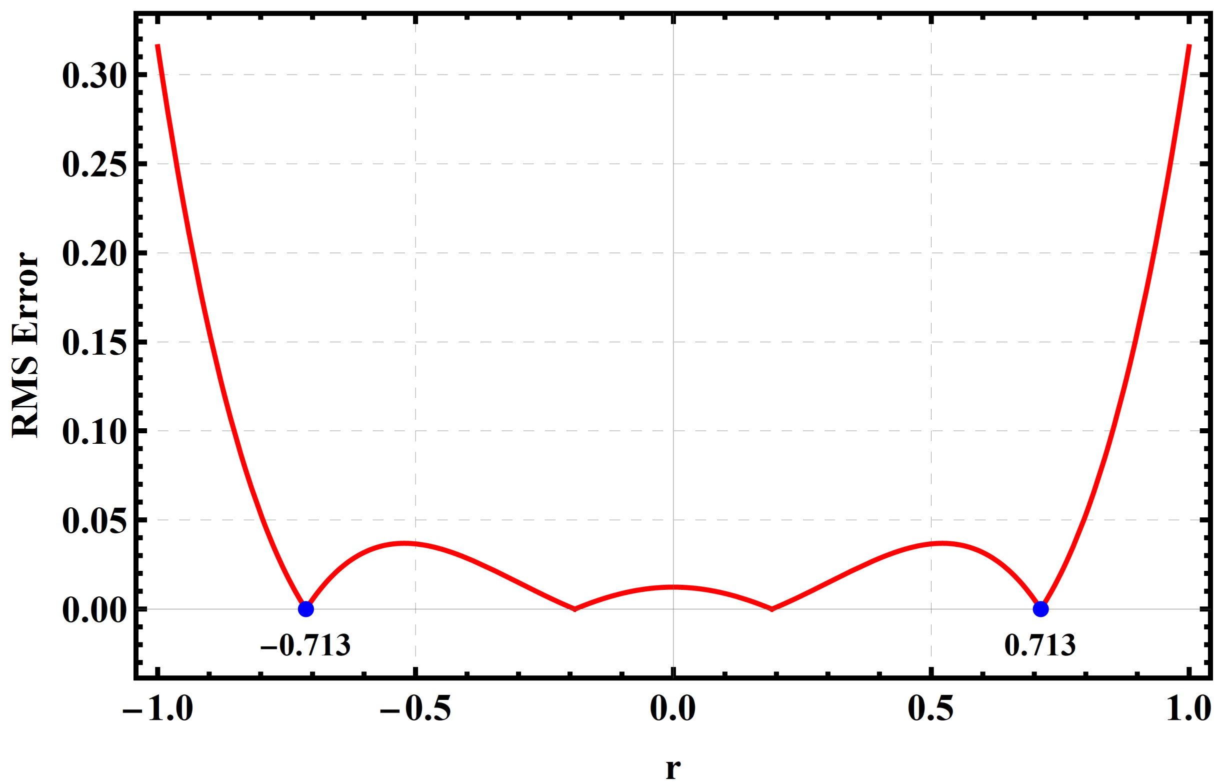

Figure 3.9: RMS error between the theoretical Zernike defocus and the measured defocus.

Chapter 4

Integration into Adaptive Optics

The DM functionality as varifocal mirror was demonstrated by integrating it into an adaptive optics system. In this chapter, step by step integration process has been discussed, the optical setup, and obtained results are given. It is shown that the DM can be a promising candidate among other varifocal mirrors, and it can advance the state-of-the-art focus scanning techniques.

4.1 Endurance of the DM

Endurance is an important parameter for DMs which shows the maximum employable power of an incident beam that the mirror surface can resist. The DM endurance was tested by exposing a 532 nm pulsed laser beam onto the mirror surface with different PRRs while the DM was not actuated, and the power of the laser beam was increased until the DM is burned. The power of the incident laser beam and the reflected beam from the DM were measured by using optical power meter.

The DM was illuminated with a 532 nm pulsed laser beam at 50 kHz and 600 kHz PRRs. In order to measure durability of the whole surface, the diameter of the incident beam was set to 3.5 mm to cover whole mirror surface area of the DM. The incident beam coming from the laser was sent directly to the mirror surface without using any additional optical components. The power of the incident beam and the reflected beam were measured using optical power meter before and after the DM, respectively. Figure 4.1 illustrates the experimental setup.

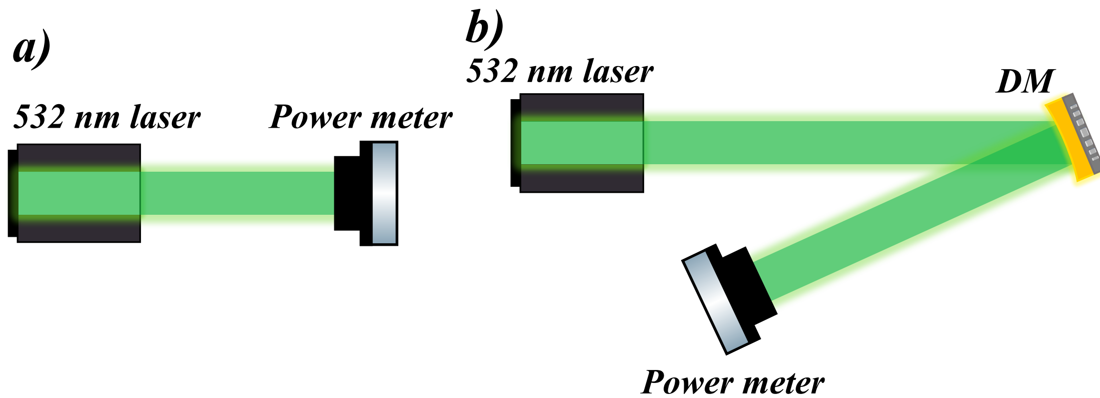

Figure 4.1: The measurements of the power of the laser beam a) before, and b) after the DM.

The reflectance of the DM surface was calculate using the formula:

$$\text{Reflectance} = \frac{\text{Power of Reflected Beam}}{\text{Power of Incident Beam}} \tag{4.1}$$

and the energy of the incident laser beam per pulse was calculated as

$$\text{Energy (J)} = \frac{\text{Power of the Beam (W)}}{\text{PRR of the laser (Hz)}} \tag{4.2}$$

It was observed that the DM can resist 50 kHz PRR incident laser beam when the attenuator of the laser is opened fully. However, the DM was burnt when the power of the 600 kHz incident beam was reached to 3500 nJ energy with full attenuation. The results of these measurements are shown in the Figure 4.2.

It can be seen from the Figure 4.2 that the reflectance of the beam from the DM surface is smaller than the theoretical value of the gold reflectivity at 532 nm wavelength. This is because of the illuminating laser onto the mirror surface with greater diameter than the mirror plate. These results demonstrated that the DM can be operated in many applications such as microscopy, ophthalmology, and OCT safely without burning.

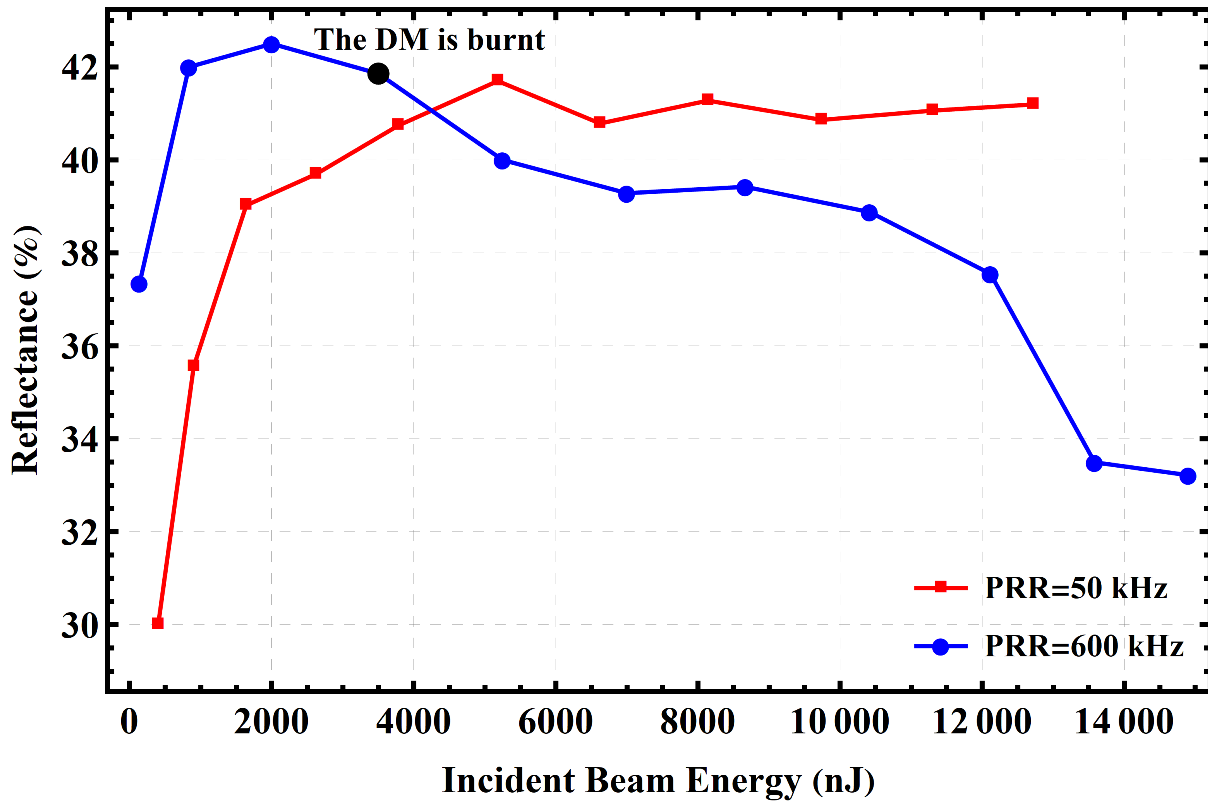

Figure 4.2: Results of the endurance test of the DM, the black dot shows the place where the DM is burnt.

4.2 Optical Characteristics

Optical characteristics of the DM was also investigated. First, the reflectivity of the mirror surface was measured by illuminating a 532 nm pulsed laser beam while the DM is grounded. The incident beam is collimated to 625 µm beam waist. The reflectance of the surface was measured as 65% using optical power meter. This agrees with measured value of the gold reflectivity at 532 nm wavelength in the literature, shown in the Figure 4.3.

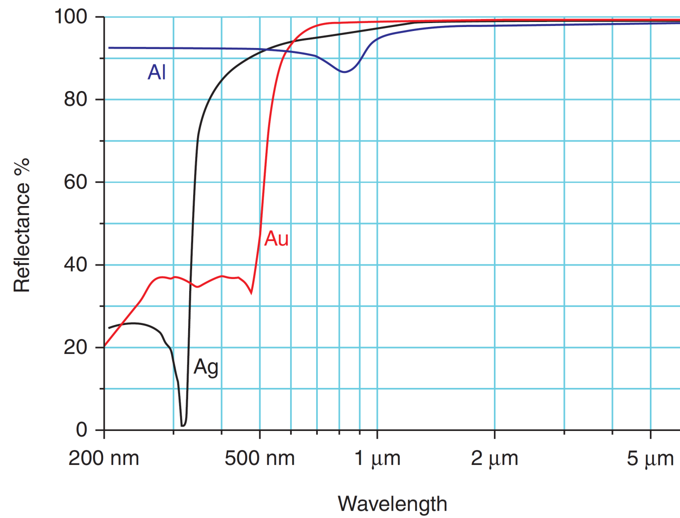

Figure 4.3: The measured value of the gold reflectivity [62].

Further, the profile of the reflected laser beam was analysed by using an optical beam profiler camera. The results showed that the measured profile of the reflected beam matches with the Gaussian distribution 92.8% and 93.5% along the horizontal and vertical axes, respectively. The results are shown in the Figure 4.4.

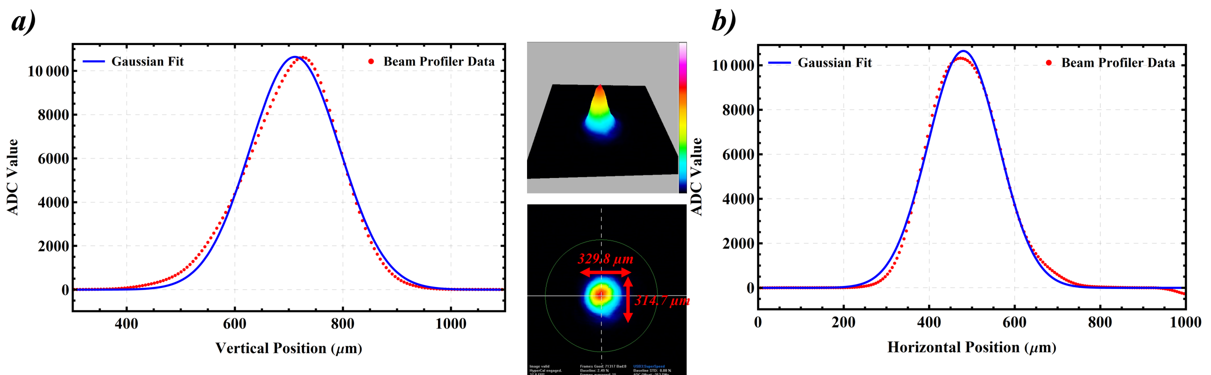

Figure 4.4: a) Horizontal and b) vertical profiles of the laser beam reflected from the DM (red dots) compared to a Gaussian fit (blue line). Insets shows the 2D and 3D profiles of the reflected beam.

4.3 Varifocal Mirror

The DM functionality as a varifocal mirror was demonstrated by integrating it into an adaptive optics system shown in the Figure 4.5. The PRR of the laser beam was set to 16 kHz to synchronize it with the oscillations of the defocus mode. The laser beam was collimated to 625 µm beam waist, again. The beam waist of the reflected laser beam was measured using a beam profiler camera at 14 equally spaced distances from the DM.

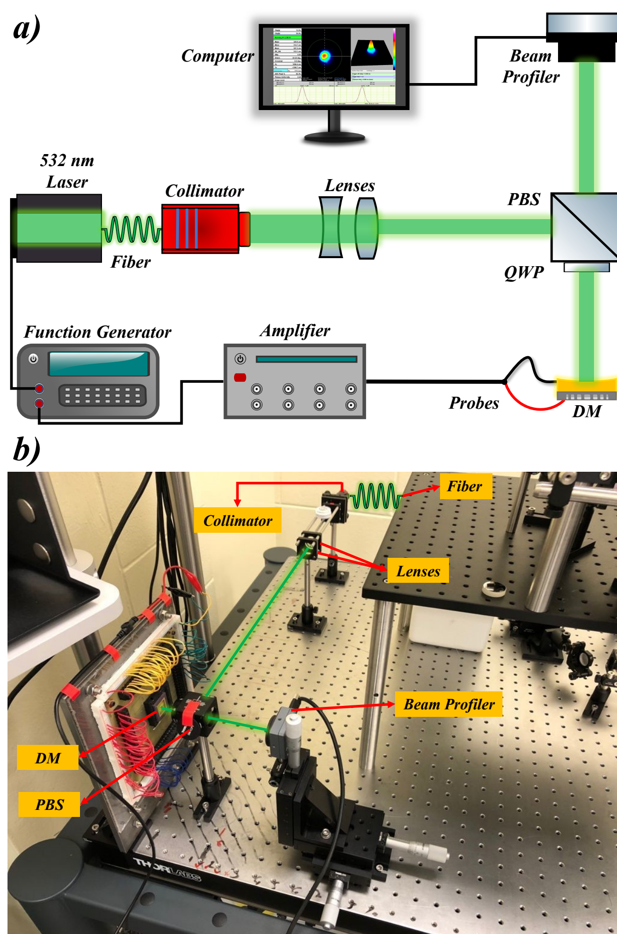

Figure 4.5: a) A schematic and b) a picture of the adaptive optics experimental setup.

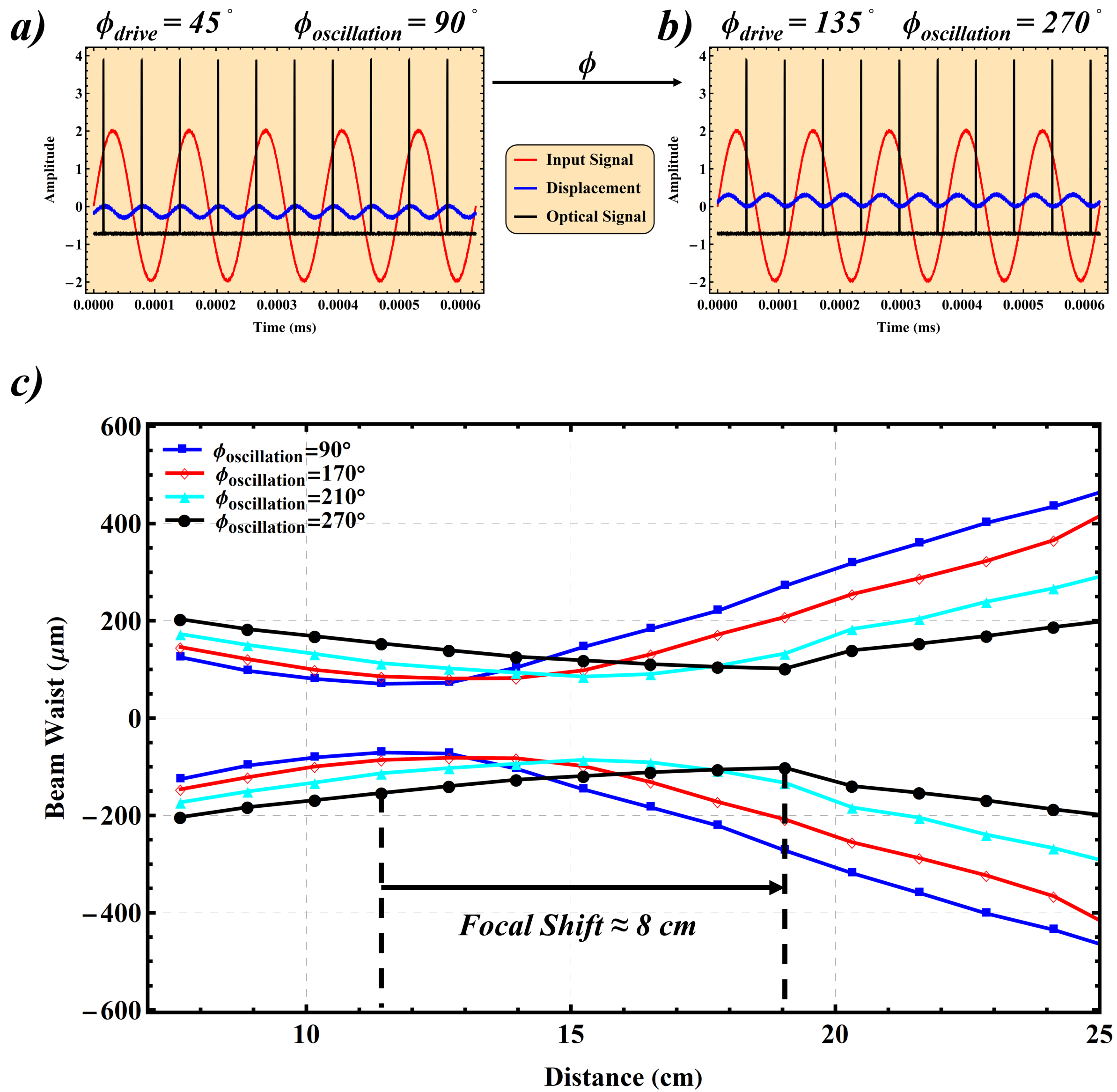

Figure 4.6: Drive signal of the DM (red line), pulse signal of the laser beam (blue line), and DM displacement (black line) for a) $\phi_{\text{drive}} = 45°$ and b) $\phi_{\text{drive}} = 135°$. c) The measured beam waist of the reflected beam at 14 equally spaced points measured from the DM.

The focal point of the reflected beam was shifted by changing the radius of curvature of the DM surface profile. The DM curvature was manipulated by changing the phase angle between the drive signal of the DM and pulsed signal of the incident laser beam, ϕ_{drive}. Same function generator was used for the pulse signal of the laser beam, and the drive signal of the DM, and both signals are triggered. So, ϕ_{drive} was changed easily by using the phase knob on the function generator. A θ° amount of change between input signal of the DM and pulsed signal of the laser beam, ϕ_{drive}, corresponds $2\,\theta^{\circ}$ change between the DM oscillation signal and pulse signal of the laser beam, $\phi_{\text{oscillation}}$, due to quadratic relationship between the voltage signal and electrostatic force. The reflected beam profiles were recorded for 4 values of ϕ_{drive} 45°, 85°, 105°, and 135° which correspond $\phi_{\text{oscillation}} = 90°$, 170°, 210°, and 270°. The measured waist of the reflected beam show that a focal shift of 8 cm was realized as the focal length move from 11 cm to 19 cm away from the DM, Figure 4.6(c), when ϕ_{drive} increased from 45° to 135°, Figure 4.6(a) and Figure 4.6(b).

Chapter 5

Conclusions and Future Work

5.1 Conclusions

Recent advancements in AO have highlighted the need of miniaturized, fast, easy-driven and low-cost DMs as an alternative to current DMs. A continuous resonant MEMS DM was introduced to address this demand, and to advance the state-of-the-art wavefront correction elements in AO. Electrostatic actuation mechanism was deployed to deform mirror surface dynamically by driving the DM at resonance via single harmonic voltage signal. This approach enables switching among Zernike modes in real-time during scanning. It also eliminates the need for individually accessible electrodes, the use of complex control algorithms, and associated hardware. REA minimizes the required electrode count, and increases the stroke distance by hitting the resonance and benefiting form dynamic amplification. Therefore, it allows to achieve simple device architecture, and to reduce fabrication cost. The DM represents a miniaturized, easy-driven, and fast modulating alternative to previous DMs.

The design of the mirror plate, support beams, and electrodes were investigated by using FEM analysis. The DM was fabricated using Micra-GEM-Si microfabrication process. Experimental characterization were conducted to identify the natural frequencies of the mirror plate, and to extract the corresponding mode shapes. The mirror surface evolution during the defocus mode oscillations were measured to obtain surface profiles and the strokes at different phase angles. This data was used to control the curvature of the DM surface while it oscillates in this mode. The endurance of the mirror surface was tested to investigate the maximum power provided by the incident photons that the DM surface can resist without getting any damage. The optical characteristics of the mirror surface was also investigated to analyse the performance of the DM surface, and the quality of the reflected beam. To demonstrate its ability as a DM, it is integrated

into an optical system. The defocus mode of the DM was used as varifocal mirror to shift the focal point of a 532 nm pulsed laser beam. The surface curvature was controlled by changing the phase angle between the pulse signal of the incident beam and the drive signal of the DM. It was demonstrated that the focal point of the pulsed laser beam was scanned between the focal lengths of 11 cm and 19 cm per defocus oscillation.

The presented DM is able to replicate eight low and high order Zernike modes. It can be integrated into various optical systems to compensate wavefront aberrations, and to increase the resolution and contrast of the images. The mirror can be a promising candidate for reflective-type wavefront correction techniques in AO.

5.2 Future Work

As a further work, the DM can be integrated into different optical systems such as two-photon microscopy, multi-photon microscopy and photoacoustic microscopy to be used as varifocal mirror for various applications such as axial scanning and 3D multiwavelength imaging. Moreover, its ability to correct wavefront aberrations can be demonstrated by integrating it into an AO system to correct different aberrations.

The design of the presented DM has an air gap of 20 µm due to imposed fabrication constraints. The new fabrication methodology can be developed and implemented to reduce the air gap distance. That will allow to reach higher strokes, and improve the performance.

A complete mathematical model can be developed to investigate the deformation characteristics of the circular plates when REA is used. That can allow to enhance the design with deeper understanding.

References

[1] J. Sasián, *Introduction to Aberrations in Optical Imaging Systems*. Cambridge University Press, 2012.

[2] M. M. Sinjab and A. B. Cummings, *Customized Laser Vision Correction*. Springer, 2018.

[3] E. Hecht, *Optics*. Springer, 2017.

[4] Wikipedia contributors, "Spherical aberration," 2021.

[5] A. Romano, *Geometric Optics Theory and Design of Astronomical Optical Systems Using Mathematica*. Modeling and Simulation in Science, Engineering and Technology, Springer International Publishing, 2016.

[6] Edmun Optics, "Chromatic and monochromatic optical aberrations," 2021.

[7] Wikipedia contributors, "Optical aberration," 2021. [Online; accessed 6-December-2021].

[8] Wikipedia contributors, "Chromatic aberration," 2021.

[9] M. J. Booth, "Adaptive optics in microscopy," *Philosophical Transactions of the Royal Society A: Mathematical, Physical and Engineering Sciences*, vol. 365, no. 1861, pp. 2829–2843, 2007.

[10] J. C. C. López, A. B. Díaz, O. J. T. Rojas, and Y. T. Moreno, "Atmospheric turbulence temperature on the laser wavefront properties," *Journal of Physics: Conference Series*, vol. 850, p. 012001, 2017.

[11] G.-m. Dai, *Wavefront Optics for Vision Correction*, vol. 179. SPIE Press, 2008.

[12] Y. Ren, H. Huang, G. Xie, N. Ahmed, Y. Yan, B. I. Erkmen, N. Chandrasekaran, M. P. J. Lavery, N. K. Steinhoff, M. Tur, S. Dolinar, M. Neifeld, M. J. Padgett, R. W. Boyd, J. H. Shapiro, and A. E. Willner, "Atmospheric turbulence effects on the performance of a free

space optical link employing orbital angular momentum multiplexing," *Opt. Lett.*, vol. 38, pp. 4062–4065, Oct 2013.

[13] M. J. Booth, "Adaptive optical microscopy: the ongoing quest for a perfect image," *Light: Science & Applications*, vol. 3, no. 4, pp. e165–e165, 2014.

[14] J. Schwiegerling *et al.*, "Field guide to visual and ophthalmic optics," Spie Bellingham, Washington, USA, 2004.

[15] V. Lakshminarayanan and A. Fleck, "Zernike polynomials: a guide," *Journal of Modern Optics*, vol. 58, no. 7, pp. 545–561, 2011.

[16] L. K. Young, G. D. Love, and H. E. Smithson, "Different aberrations raise contrast thresholds for single-letter identification in line with their effect on cross-correlation-based confusability," *Journal of vision*, vol. 13, no. 7, pp. 12–12, 2013.

[17] C. Zhao and J. H. Burge, "Orthonormal vector polynomials in a unit circle, part i: basis set derived from gradients of zernike polynomials," *Optics Express*, vol. 15, no. 26, pp. 18014–18024, 2007.

[18] M. J. Booth, M. A. Neil, R. Juškaitis, and T. Wilson, "Adaptive aberration correction in a confocal microscope," *Proceedings of the National Academy of Sciences*, vol. 99, no. 9, pp. 5788–5792, 2002.

[19] R. Shannon, *Applied Optics and Optical Engineering V8*, vol. 8. Elsevier, 2012.

[20] JPE Innovations, "Zernike modes & deformable mirrors," 2021.

[21] J. A. Kubby, *Adaptive optics for biological imaging*. CRC press, 2013.

[22] R. Tyson, *Principles of Adaptive Optics*. CRC Press, 2011.

[23] R. A. Fisher, *Optical phase conjugation*. Academic press, 2012.

[24] R. K. Tyson and B. W. Frazier, *Conventional Adaptive Optics System*, pp. 1–2. SPIE.

[25] M. J. Booth, "Adaptive optics in microscopy," *Optical and Digital Image Processing: Fundamentals and Applications*, pp. 295–322, 2011.

[26] P. Hariharan, "Chapter 1 - interferometry: Its development," in *Optical Interferometry (Second Edition)* (P. Hariharan, ed.), pp. 1–8, San Diego: Academic Press, second edition ed., 2003.

[27] P. S. Salter and M. J. Booth, “Adaptive optics in laser processing,” *Light: Science & Applications*, vol. 8, no. 1, pp. 1–16, 2019.

[28] Edmun Optics, “Introduction to adaptive optics and deformable mirrors,” 2021.

[29] R. Davies and M. Kasper, “Adaptive optics for astronomy,” *Annual Review of Astronomy and Astrophysics*, vol. 50, pp. 305–351, 2012.

[30] N. Ji, “Adaptive optical fluorescence microscopy,” *Nature methods*, vol. 14, no. 4, pp. 374–380, 2017.

[31] A. Roorda and J. L. Duncan, “Adaptive optics ophthalmoscopy,” *Annual review of vision science*, vol. 1, pp. 19–50, 2015.

[32] E. Akyol, A. M. Hagag, S. Sivaprasad, and A. J. Lotery, “Adaptive optics: principles and applications in ophthalmology,” *Eye*, vol. 35, no. 1, pp. 244–264, 2021.

[33] B. Hermann, E. Fernández, A. Unterhuber, H. Sattmann, A. Fercher, W. Drexler, P. Prieto, and P. Artal, “Adaptive-optics ultrahigh-resolution optical coherence tomography,” *Optics letters*, vol. 29, no. 18, pp. 2142–2144, 2004.

[34] T.-H. Chen, R. Fardel, and C. B. Arnold, “Ultrafast z-scanning for high-efficiency laser micro-machining,” *Light: Science & Applications*, vol. 7, no. 4, pp. 17181–17181, 2018.

[35] M. A. Abozaid *et al.*, “The use of adaptive optics for retinal imaging with microscopic resolution,” *Journal of the Egyptian Ophthalmological Society*, vol. 109, no. 4, p. 145, 2016.

[36] T. G. Bifano, J. Perreault, R. K. Mali, and M. N. Horenstein, “Microelectromechanical deformable mirrors,” *IEEE Journal of selected topics in quantum electronics*, vol. 5, no. 1, pp. 83–89, 1999.

[37] P.-Y. Madec, “Overview of deformable mirror technologies for adaptive optics and astronomy,” in *Adaptive Optics Systems III*, vol. 8447, p. 844705, International Society for Optics and Photonics, 2012.

[38] M. A. Ealey and J. A. Wellman, “Deformable mirrors: design fundamentals, key performance specifications, and parametric trades,” in *Active and Adaptive Optical Components* (M. A. Ealey, ed.), vol. 1543, pp. 36 – 51, International Society for Optics and Photonics, SPIE, 1992.

[39] M. A. Ealey and J. F. Washeba, "Continuous facesheet low voltage deformable mirrors," *Optical Engineering*, vol. 29, no. 10, pp. 1191–1198, 1990.

[40] J.-C. Sinquin, J.-M. Lurçon, and C. Guillemard, "Deformable mirror technologies for astronomy at cilas," in *Adaptive optics systems*, vol. 7015, p. 70150O, International Society for Optics and Photonics, 2008.

[41] R. Biasi, D. Gallieni, P. Salinari, A. Riccardi, and P. Mantegazza, "Contactless thin adaptive mirror technology: past, present, and future," in *Adaptive Optics Systems II*, vol. 7736, p. 77362B, International Society for Optics and Photonics, 2010.

[42] T. Bifano, "Mems deformable mirrors," *Nature photonics*, vol. 5, no. 1, pp. 21–23, 2011.

[43] D. J. Bell, T. Lu, N. A. Fleck, and S. M. Spearing, "Mems actuators and sensors: observations on their performance and selection for purpose," *Journal of Micromechanics and Microengineering*, vol. 15, no. 7, p. S153, 2005.

[44] R. E. Morgan, E. S. Douglas, G. W. Allan, P. Bierden, S. Chakrabarti, T. Cook, M. Egan, G. Furesz, J. N. Gubner, T. D. Groff, *et al.*, "Mems deformable mirrors for space-based high-contrast imaging," *Micromachines*, vol. 10, no. 6, p. 366, 2019.

[45] J. B. Stewart, T. G. Bifano, P. Bierden, S. Cornelissen, T. Cook, and B. M. Levine, "Design and development of a 329-segment tip-tilt piston mirror array for space-based adaptive optics," in *MEMS/MOEMS Components and Their Applications III*, vol. 6113, p. 61130O, International Society for Optics and Photonics, 2006.

[46] Boston Micrmachines Corporation, "Hex class deformable mirrors," 2021. Tec. rep.

[47] M. A. Helmbrecht, M. He, T. Juneau, M. Hart, and N. Doble, "Segmented mems deformable-mirror for wavefront correction," in *Optomechatronic Micro/Nano Devices and Components II*, vol. 6376, p. 63760D, International Society for Optics and Photonics, 2006.

[48] Boston Micrmachines Corporation, "Ptt489 dm system sspecifications," 2021. Tec. rep.

[49] C. J. Kempf, M. A. Helmbrecht, and M. Besse, "Adaptive optics control system for segmented mems deformable mirrors," in *MEMS Adaptive Optics IV*, vol. 7595, p. 75950M, International Society for Optics and Photonics, 2010.

[50] S. Manzanera, M. A. Helmbrecht, C. J. Kempf, and A. Roorda, "Mems segmented-based adaptive optics scanning laser ophthalmoscope," *Biomedical optics express*, vol. 2, no. 5, pp. 1204–1217, 2011.

[51] T. G. Bifano, J. A. Perreault, and P. A. Bierden, "Micromachined deformable mirror for optical wavefront compensation," in *High-Resolution Wavefront Control: Methods, Devices, and Applications II*, vol. 4124, pp. 7–14, International Society for Optics and Photonics, 2000.

[52] S. Cornelissen, P. Bierden, and T. Bifano, "A 4096 element continuous facesheet mems deformable mirror for high-contrast imaging," in *MEMS Adaptive Optics II*, vol. 6888, p. 68880V, International Society for Optics and Photonics, 2008.

[53] K. Banerjee, P. Rajaeipour, H. Zappe, and Ç. Ataman, "A 37-actuator polyimide deformable mirror with electrostatic actuation for adaptive optics microscopy," *Journal of Micromechanics and Microengineering*, vol. 29, no. 8, p. 085005, 2019.

[54] Y. Hishinuma and E.-H. Yang, "Piezoelectric unimorph microactuator arrays for single-crystal silicon continuous-membrane deformable mirror," *Journal of microelectromechanical systems*, vol. 15, no. 2, pp. 370–379, 2006.

[55] J. Pribošek, M. Bainschab, A. Piot, and M. Moridi, "Aspherical high-speed varifocal piezoelectric mems mirror," in *2021 21st International Conference on Solid-State Sensors, Actuators and Microsystems (Transducers)*, pp. 1088–1091, 2021.

[56] B. Park, "Development of a low voltage and large stroke mems-based lorentz force continuous deformable polymer mirror system," 2018. PhD Thesis.

[57] M. J. Booth, "Adaptive optical microscopy: the ongoing quest for a perfect image," *Light: Science & Applications*, vol. 3, no. 4, pp. e165–e165, 2014.

[58] M. A. Ealey and J. A. Wellman, "Deformable mirrors: design fundamentals, key performance specifications, and parametric trades," in *Active and Adaptive Optical Components*, vol. 1543, pp. 36–51, International Society for Optics and Photonics, 1992.

[59] A. Kamel, "Resonant adaptive mirrors," 2020. PhD Thesis.

[60] I. W. Jung, Y. Peter, E. Carr, J.-S. Wang, and O. Solgaard, "Single-crystal-silicon continuous membrane deformable mirror array for adaptive optics," in *IEEE/LEOS International Conference on Optical MEMS and Their Applications Conference, 2006.*, pp. 152–153, 2006.

[61] A. Liotard and F. Zamkotsian, "Static and dynamic micro deformable mirror characterization by phase-shifting and time-averaged interferometry," in *Optical Fabrication, Metrology, and Material Advancements for Telescopes* (E. Atad-Ettedgui and P. Dierickx, eds.), vol. 5494, pp. 480 – 491, International Society for Optics and Photonics, SPIE, 2004.

[62] Wikipedia contributors, “Reflectance,” 2021.